Efficient and Accurate Computation of Non-Negative Anisotropic Group Scattering Cross Sections for Discrete Ordinates and Monte Carlo Radiation Transport

David W. Gerts

**EFFICIENT AND ACCURATE
COMPUTATION OF NON-NEGATIVE
ANISOTROPIC SCATTERING CROSS
SECTIONS FOR DISCRETE ORDINATES
AND MONTE CARLO TRANSPORT**

DISSERTATION

David W. Gerts, Captain, USAF

**DEPARTMENT OF THE AIR FORCE
AIR UNIVERSITY**

AIR FORCE INSTITUTE OF TECHNOLOGY

Wright-Patterson Air Force Base, Ohio

Report Documentation Page

Report Date 24 July 02	Report Type Final	Dates Covered (from... to) April 99 - Jul 02

Title and Subtitle Efficient and Accurate Computation of Non-Megative Anisotropic Group Scattering Cross Sections for Discrete Ordinates and Monte Carlo Radiation Transport	Contract Number
	Grant Number
	Program Element Number

Author(s) Capt Daid W. Gerts, USAF	Project Number
	Task Number
	Work Unit Number

Performing Organization Name(s) and Address(es) Air Force Institute of Technology Graduate School of Engineering and Management (AFIT/EN) 2950 P Street, Bldg 640 WPAFB OH 45433-7765	Performing Organization Report Number AFIT/DS/ENP/02-04

Sponsoring/Monitoring Agency Name(s) and Address(es) Air Forec Technical Applications Center ATTN: Maj Jeremy Holtgrave Patrick AFB FL 32925	Sponsor/Monitor's Acronym(s)
	Sponsor/Monitor's Report Number(s)

Distribution/Availability Statement
Approved for public release, distribution unlimited

Supplementary Notes

Abstract
A new method for approximating anisotropic, multi-group scatter cross sections for use in discretized and Monte Carlo multi-group neutron transport is presented. The new method eliminates unphysical artifacts such as negative group scatter cross sections and falsely positive cross sections. Additionally, when combined with the discrete elements angular quadrature method, the new cross sections eliminate the lack of angular support in the discrete ordinates quadrature method. The new method generates piecewise-average group-to-group scatter cross sections. The accuracy and efficiency for calculating the discrete elements cross sections has improved by many orders of magnitude compared to DelGrande and Mathews previous implementation. The new cross sections have extended the discrete elements method to all neutron-producing representations in the Evaluated Nuclear Data Files. The new cross section method has been validated and tested with the cross section generation code, NJOY. Results of transport calculations using discrete elements, discrete ordinates, and Monte Carlo methods for two, one-dimensional slab geometry problems are compared.

Subject Terms
Boltzmann Equation, Neutron Transport Theory, Numerical Methods, Radiation Transport, Radiation Shielding, Anisotropic Cross Sections, Multi-Group Theory

Report Classification unclassified	Classification of this page unclassified

Classification of Abstract	**Limitation of Abstract**
unclassified	UU

Number of Pages
136

EFFICIENT AND ACCURATE COMPUTATION OF NON-NEGATIVE ANISOTROPIC GROUP SCATTERING CROSS SECTIONS FOR DISCRETE ORDINATES AND MONTE CARLO RADIATION TRANSPORT

DISSERTATION

Presented to the Faculty
Graduate School of Engineering and Management
Air Force Institute of Technology
Air University
Air Education and Training Command
in Partial Fulfillment of the Requirements for the
Degree of Doctor of Philosophy

David W. Gerts, B.S., B.S., M.S.
Captain, USAF

July 2002

EFFICIENT AND ACCURATE COMPUTATION OF
NON-NEGATIVE ANISOTROPIC GROUP
SCATTERING CROSS SECTIONS FOR
DISCRETE ORDINATES AND MONTE CARLO
RADIATION TRANSPORT

David W. Gerts, B.S., B.S., M.S.
Captain, USAF

Approved:

<u>Date</u>

_____   _____

Kirk A. Mathews (Advisor)

_____   _____

James T. Moore (Dean's Representative)

_____   _____

Charles J. Bridgman (Member)

_____   _____

Dennis W. Quinn (Member)

Accepted:

_____   _____

Robert A. Calico, Jr.   Date
Dean, Graduate School of Engineering and Managment

Acknowledgements

I would like to acknowledge my wife as the source of my support throughout my time at AFIT. She has always given me love and patience throughout my five years at AFIT. I cannot ever thank her enough.

My children have been the source of excitement and fun for the past five years. My daughter was born while I was just beginning the long road of the Ph.D. program and my son has been there ever since I started graduate school. Both of my parents have given me the encouragement and education that have made this degree possible. I appreciate both of their support.

I would finally like to acknowledge my committee. My research adviser, Dr. Mathews, has given an amazing amount of time, effort, and patience. I have learned from, partnered with, and been mentored by him. I thank him for everything he has taught me.

My dissertation research has been fun, exciting, and even excruciatingly painful at times. I am glad that I had the time in my life to simply pursue knowledge and I thank the Air Force for allowing me (and paying me) to go to school. It has been a continuous growing experience for me.

Table of Contents

List of Figures

List of Algorithms

List of Tables

List of Acronyms

Acronym	Meaning
ACE	A Compact ENDF
BTE	Boltzmann Transport Equation
DE_n	Discrete Elements quadrature set with n elements
DD	Diamond Difference
EC	Exponential Characteristic
ENDF/B-VI	Evaluated Nuclear Data Files version B-VI
IMSL	International Mathematics Software Library
MCNP	Monte Carlo Neutron-Photon transport code
NJOY	Nuclear processing code system
PAX_K	Piecewise-average group scattering cross sections
P_l	Truncated Legendre expansion through order l
S_n	Discrete ordinates quadrature set with n ordinates

Summary of Variables

Variable	Summary	Page Reference
ΔE_g	Energy group for group (g)	4
$\Delta \Omega_n$	Element of solid angle defining discrete element (n)	5
$\delta\left(m - \hat{\Omega}'\cdot\hat{\Omega}\right)$	Delta distribution function	19
$F(E)$	Spectral energy function	4
ϕ	Scalar (all-angle) flux	4
m	Cosine of the scatter angle	19
m_n	Ordinate (n) for 1-D discrete ordinates transport	5
σ_g^t	Total cross section for group (g)	4
σ^s	Continuous scatter cross section	4
$\sigma_{g' g}^s$	Scatter cross section for incident group (g') to secondary group (g)	4
$\sigma_{n'n,g'g}^s$	Group-to-group scatter cross section for either discrete ordinates or discrete elements	5
$\sigma_{l,g'g}$	l^{th} Legendre moment group cross section	9
$\overline{\sigma}_{g'g,k}$	Average group-to-group scatter cross section in k^{th} interval of m	21
σ^*	Doppler broadened effective cross section	
$\hat{\Omega}$	Angular direction	4
$\overline{\Omega}_n$	First moment of angular direction	5
ψ_g	Group (g) angular flux	4
$\psi_{n,g}$	Group (g), element/ordinate (n) angular flux	5
A	Ratio of atomic mass to neutron mass	32
E'	Incident energy	4
E_s	Secondary energy after either elastic or level inelastic scatter	32

Abstract

A new method for approximating anisotropic, multi-group scatter cross sections for use in discretized and Monte Carlo multi-group neutron transport is presented. The new method eliminates unphysical artifacts such as negative group scatter cross sections and falsely positive cross sections. Additionally, when combined with the discrete elements angular quadrature method, the new cross sections eliminate the lack of angular support in the discrete ordinates quadrature method.

The new method generates piecewise-average group-to-group scatter cross sections. The accuracy and efficiency for calculating the discrete elements cross sections has improved by many orders of magnitude compared to DelGrande and Mathews (7) previous implementation. The new cross sections have extended the discrete elements method to all neutron-producing representations in the Evaluated Nuclear Data Files (13).

The new cross section method has been validated and tested with the cross section generation code, NJOY (13). Results of transport calculations using discrete elements, discrete ordinates, and Monte Carlo methods for two, one-dimensional slab geometry problems are compared.

Efficient and Accurate Computation of Non-negative Anisotropic Group Scattering Cross Sections for Discrete Ordinates and Monte Carlo Radiation Transport

I. Introduction

The conventional practice for evaluating the discretized, multi-group Boltzmann transport equation is the discrete ordinates angular quadrature method with truncated Legendre expansions representing the multi-group cross sections. The truncated Legendre expansions for the cross sections can lead to negative scatter cross sections. These negative scatter cross sections can give rise to negative scatter sources, which can lead to inaccurate, negative, and thereby unphysical angular flux solutions. The unphysical angular flux solutions motivated many to rely on comparatively expensive Monte Carlo transport simulations.

Discrete element cross sections, recently introduced by DelGrande and Mathews (7), eliminate the negative scatter cross section artifacts, but efficient and accurate techniques for generating these discrete elements cross sections have not been available.

The cross sections for multi-group Monte Carlo transport also inherit inaccuracies by attempting to reconstruct non-negative cross sections from truncated Legendre expansions (5, 11).

In the work presented here, I have developed algorithms, implemented, and then validated a code to generate multi-group cross sections. The code improves the efficiency of the calculation of discrete elements cross sections for discrete ordinates transport methods. Furthermore, it provides accurate representations suitable for multi-group Monte Carlo transport methods. The utility of these cross sections is demonstrated using various discrete ordinates transport calculations with two test problems.

I.1: MULTI-GROUP BOLTZMANN TRANSPORT EQUATION

The multi-group approximation for the Boltzmann transport equation (BTE) is

$$\hat{\Omega}\cdot\nabla\psi_g\left(\vec{r},\hat{\Omega}\right) + \sigma_g^t\left(\vec{r}\right)\psi_g\left(\vec{r},\hat{\Omega}\right) = q_g\left(\vec{r},\hat{\Omega}\right) + \sum_{g'=1}^{G}\int d\hat{\Omega}'\sigma_{g'g}^s\left(\vec{r},\hat{\Omega}'\cdot\hat{\Omega}\right)\psi_{n,g'}\left(\vec{r},\hat{\Omega}'\right) \quad (1)$$

The symbols in this dissertation are summarized in the table of symbols in the beginning and described in appendix A. The notation used in this dissertation follows the conventions of Lewis and Miller (7). The subscripts in the multi-group equation designate the group (g) and later the ordinate or element (n). The spatial dependence is suppressed in all further equations. The superscript designates the type of scatter or the total cross section. For further development, the multi-group scatter cross section is defined as

$$\sigma_{g'g}^s\left(\hat{\Omega}'\cdot\hat{\Omega}\right) = \frac{\displaystyle\int_{\Delta E_{g'}} dE' \int_{\Delta E_g} dE\, \sigma^s\left(E'\to E, \hat{\Omega}'\cdot\hat{\Omega}\right)F\left(E'\right)}{\displaystyle\int_{\Delta E_{g'}} dE'\, F\left(E'\right)}, \quad (2)$$

where $F\left(E'\right)$ is the energy-dependent spectral weighting function.

The multi-group cross section can be further discretized in angle into either the discrete ordinates approximation or the discrete elements approximation. For discrete elements, discrete ordinates, or multi-group Monte Carlo, the representation of the multi-group cross section defined in equation (2) should have the following desirable attributes.

1. Non-negative, but not strictly positive
2. Account for all incident to secondary energy group pairs for all scatter mechanisms
3. Efficiently computed
4. Computed within user-specified accuracy
5. Use a representation that is flexible enough to support Monte Carlo, discrete ordinates, and discrete elements multi-group transport methods

Multi-group Monte Carlo transport is not tested in this work and is presented clearly in the reference for MCNP (2). The discrete elements and the discrete ordinates methods are introduced and compared.

The discrete ordinates method samples the angular flux at given directions and uses a quadrature rule to integrate the angular flux to get the scalar flux.

The one-dimensional, slab geometry, multi-group discrete ordinates equation is

$$\mu_n \frac{d}{dx}\psi_{n,g} + \sigma^t\,\psi_{n,g}(x) = q_{n,g} + \sum_{n'}\sum_{g'}\sigma_{n'n,g'g}\,\psi_{n'g'}, \tag{3}$$

where the ordinate-to-ordinate, group-to-group scatter cross section is

$$\sigma_{n'n,g'g} = \frac{\displaystyle\int_{\Delta E_{g'}} dE'\int_{\Delta E_g} dE\,\sigma^s\!\left(E'\to E,\hat{W}_{n'}\cdot\hat{W}_n\right)\Phi(E')}{\displaystyle\int_{\Delta E_{g'}} dE'\,\Phi(E')}. \tag{4}$$

Discrete ordinates conventionally uses the Legendre moments of the cross sections, $\sigma_{l,g'g}$, directly by computing the Legendre moments of the angular flux, f_l, and combining those with the cross section Legendre moments to get the scattering source for each ordinate, n.

The series of approximate discrete ordinate, angular flux solutions to the multi-group BTE equation do not converge uniformly. As more points are added to the angular quadrature, the discontinuous solution (in multi-dimensional transport) for the angular flux suffers from a Gibbs phenomenon. Therefore, increasing the number of ordinates used in a solution does not guarantee a better answer.

The discrete ordinates approximation can also skip energy groups in the down-scatter arising from an incomplete angular quadrature approximation, called lack of angular support. DelGrande and Mathews (7) gave an example of the lack of angular support for discrete ordinates for multi-group scatter cross sections that skipped 109 of the next lower-energy groups out of 175 groups. Lack of angular support can lead to computational artifacts where an incorrect scalar flux is calculated.

I.3: DISCRETE ELEMENTS

The discrete elements method (7) integrates the BTE over discrete angular elements with a piece-wise constant representation of the angular flux. The scalar flux is then a sum over each of the angular flux elements. The resulting, angularly discretized, multi-group BTE has the form

$$\left[\bar{\Omega}_n \cdot \vec{\nabla} + \sigma_g^t\right]\psi_{n,g} = q_{n,g} + \sum_{n'}^{N} \sum_{g'}^{G} \sigma_{n'n,g'g}\psi_{n'g'}, \tag{5}$$

where

$$\bar{\Omega}_n = \frac{\int_{\Delta\Omega_n} d\Omega\,\hat{\Omega}}{\int_{\Delta\Omega_n} d\Omega}, \tag{6}$$

$$\psi_{n,g} = \int_{\Delta E_g} dE \int_{\Delta\Omega_n} d\Omega\,\psi\left(\hat{\Omega},E\right), \tag{7}$$

and

$$q_{n,g}(\vec{r}) = \int_{\Delta\Omega_n} d\Omega \int_{\Delta E_g} dE\, Q(\hat{\Omega},E). \tag{8}$$

DelGrande and Mathews (7) referred to the cells of the Cartesian product of the energy and direction meshes as bins. Thus, $\sigma_{n'n,g'g}$ is the cross section for scatter from bin (n',g') to bin (n,g). The bin-to-bin cross section is defined as

$$\sigma_{n'n,g'g} = \sum_{mech} \frac{\int_{\Delta\Omega_{n'}} d\Omega' \int_{\Delta\Omega_n} d\Omega \int_{\Delta E_{g'}} dE' \int_{\Delta E_g} dE\, \sigma^{mech}\left(E' \to E, \hat{\Omega}' \cdot \hat{\Omega}\right)F\left(E'\right)}{\Delta\Omega_{n'} \int_{g'} dE'\, F\left(E'\right)}. \tag{9}$$

DelGrande and Mathews (7) showed that the discrete elements approximation has several properties that are advantageous compared to the discrete ordinates approximation. The first property is the convergence of the discrete elements approximation to the solution of the spatially discretized problem because the approximation is equivalent to a Riemann integral for the scalar flux in the limit as $N \to \infty$. Therefore, as the angular mesh is refined, the refined answer is more accurate than the previous answer. Conversely, the discrete ordinates angular approximation, being based on the spherical harmonics functions, converges only point-wise and refinements in angle for discrete ordinates may not improve the scalar flux solution.

The second important property of discrete elements is complete angular support. Discrete elements have non-zero cross sections between all allowed energy groups for

all possible scatters. Again conversely, the discrete ordinates approximation need not have all possible energy groups included in the cross section representation.

I.4: MOTIVATION

Multi-group, non-negative, anisotropic scatter cross section methods for neutron transport have previously been either too expensive computationally (7) or too restrictive in application (2) to effectively implement for real materials and for any energy refinement.

I.5: GOAL OF THE RESEARCH

The goal is to develop, implement, and validate efficient and accurate computational methods for converting the Evaluated Nuclear Data Files version B-VI (ENDF/B-VI) (18) to multi-group cross sections, without an intermediate truncated Legendre expansion, in forms suitable for Monte Carlo, discrete ordinates, and discrete elements transport calculations.

I.6: SCOPE

I include the reactions in the ENDF/B-VI data where the neutrons are both incident and secondary particles. The new methods for calculating multi-group anisotropic scattering cross sections are validated and compared to other methods. The efficacy of these cross sections for discrete ordinates and discrete elements one-dimensional slab geometry, multi-group transport are evaluated.

I.7: ASSUMPTIONS AND LIMITATIONS

The approximation for Doppler broadening of the cross section used by NJOY (13) is assumed to be adequate and I use it here. Additionally, the R-Matrix, hybrid R-Matrix, Adler-Adler, and Kalbach-Mann representations of the scatter cross sections that are used for some isotopes in ENDF/B-VI are not included. They are not required for the evaluation and demonstrations presented here, and are left for a future effort. Utility of these cross sections for multi-group Monte Carlo calculations is self-evident and is not demonstrated due to time constraints. Use of these cross sections with multi-dimensional discrete ordinates and discrete elements is not demonstrated, also due to time constraints.

This work starts with the discrete elements approximation introduced by DelGrande and Mathews (7). They used Monte Carlo numerical quadrature to approximate the six dimensional integrals for the bin-to-bin cross sections. My approach is to reduce the computational cost by splitting each six dimensional integral in equation (9) into two, three-dimensional integrals and introducing a scattering cross section operator. All the necessary integrals are approximated using deterministic numerical quadratures to improve the computational efficiency and accuracy as compared to the Monte Carlo numerical estimate. User-set tolerances are used in the deterministic quadratures to ensure the desired accuracy is achieved.

II. Numerical Approximations for Scatter Cross Sections

This chapter presents numerical approximations for the scatter cross section. The conventional truncated Legendre expansions are presented first, followed by the Monte Carlo technique used by DelGrande and Mathews (7) to estimate bin-to-bin cross sections. A scatter cross section operator is introduced and is shown to recover both the truncated Legendre expansion and the bin-to-bin cross sections. An element-to-element conditional probability is introduced for the discrete elements quadrature. Piecewise-average group-to-group scatter cross sections are introduced, hereafter referred to as PAX cross sections. Finally, the failure of a point-wise method for tabulating the group-to-group cross sections is presented.

PAX_K is a symbol denoting piecewise-average cross sections with a uniform mesh of K (equal-width) intervals of m, ie K pieces. In a complete, formal usage, one could refer to DE_{12}/PAX_{64} analogously to S_{12}/P_{11}. But, as long as K is large enough that the numerical approximation is negligible, DE_{12} should suffice.

II.1: TRUNCATED LEGENDRE EXPANSIONS

Current practice is to use truncated Legendre expansions of the group-to-group cross sections in discretized neutron transport. The angular domain is typically approximated with discrete ordinates, as discussed in chapter 1. These two approximations have their own computational artifacts that are important to distinguish. The coefficients for the expansion, or the Legendre moments, are

$$s_{l,g\phi g} = \frac{\int_{-1}^{1} dm \int_{\Delta E_{g\phi}} dE\phi \int_{\Delta E_{g\phi}} dE\, s^s\left(E\phi \circledR E, m\right) F\left(E\phi\right) P_l\left(m\right)}{\int_{\Delta E_{g\phi}} dE\phi F\left(E\phi\right)}. \tag{10}$$

Having tabulated the Legendre moments through order L, the group-to-group cross section can be recovered (approximately) as

$$s_{g\phi g}\left(m\right) \approx \sum_{l=0}^{L} \frac{\left(2l+1\right)}{2} s_{l,g\phi g} P_l\left(m\right) \tag{11}$$

This approach has the advantage of compact storage. However, because the Legendre polynomials (for $l>0$) are not non-negative, the recovered cross sections can

be negative and in general have many regions of negativity. Simply increasing the order of the expansion, L, does not necessarily help, and may even exacerbate the problem in certain regions.

To show some problems with truncated Legendre expansions, I used the ^{10}B isotope with various group-to-group pairs and various energy group structures. The first two examples use the 30-energy group structure given in appendix D.2 to show that, in practice, it is not possible to select an order, L>0, to use for a material and all energy groups pairs and maintain positivity. The two examples have either negative regions for L small, but are strictly positive for larger L, or negative regions for all orders of L>0. All of the expansions for
 the cross sections, from P_0 through P_{11}, are shown on each plot and compared to the PAX$_{64}$ cross section.
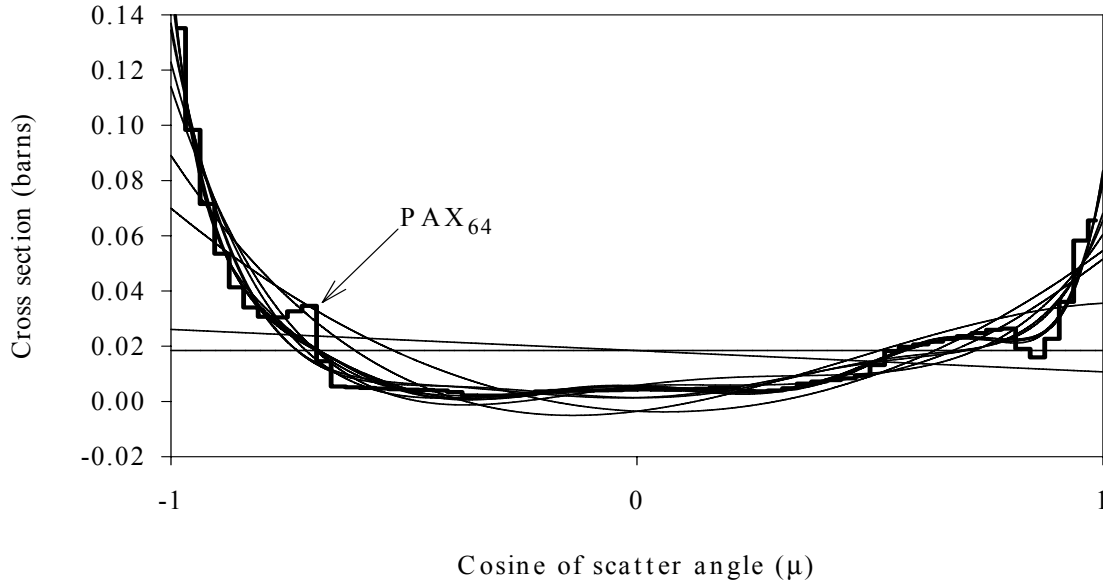
Figure 1: Negative regions for low order, L, with group 1 to group 5
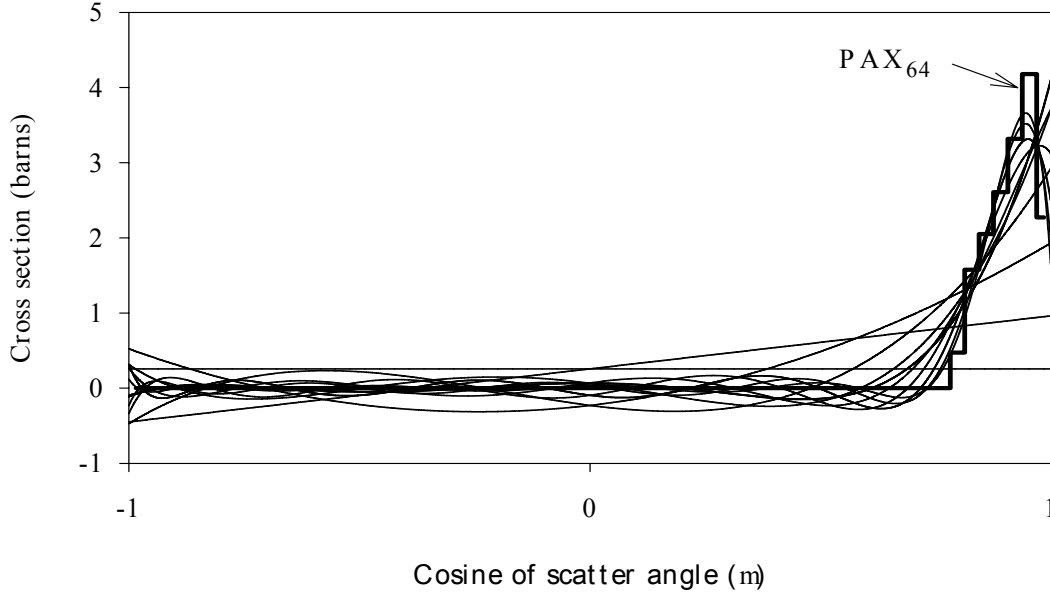
Figure 2: Negative regions for all L>0 using group 1 to group 2

These examples demonstrate that the choice of the truncation order is either dependent on the group-to-group pair, as in Figure 1, or cannot be chosen to guarantee non-negativity for L>0, as in Figure 2.

The truncated Legendre expansion through order L will often develop negative regions, as the energy group structure is refined. The ^{10}B isotope for group 1 to group 5, shown in Figure 1, is an example of the onset of negative regions as the energy group structure is refined. The example in Figure 1 favors a high-order truncated Legendre expansion because the group-to-group cross section is strictly positive and, indeed, all expansions greater than P_4 are strictly positive. In the next figures, only the P_{11} Legendre expansion is shown and compared to the PAX$_{64}$ cross sections for a refined energy group structure using 117 energy groups, described in appendix D.4. The secondary energy group, group 5, has been refined into four groups of equal width in lethargy, with the incident energy group held constant.
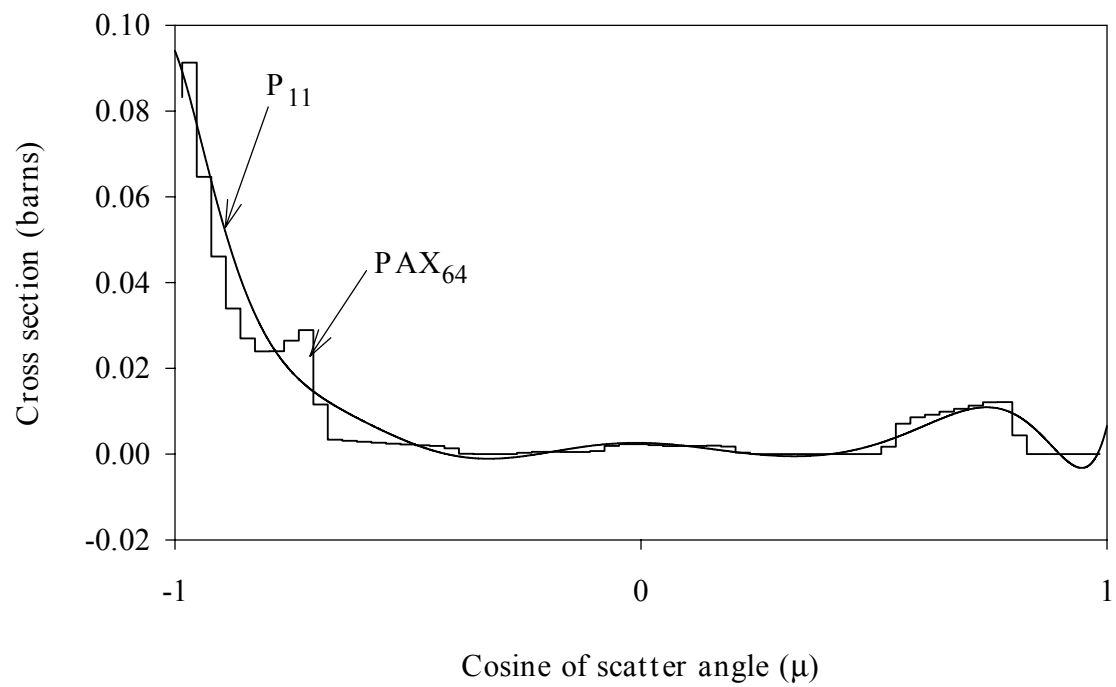
Figure 3: ^{10}B cross section for group 1 to 14 in 117-group structure
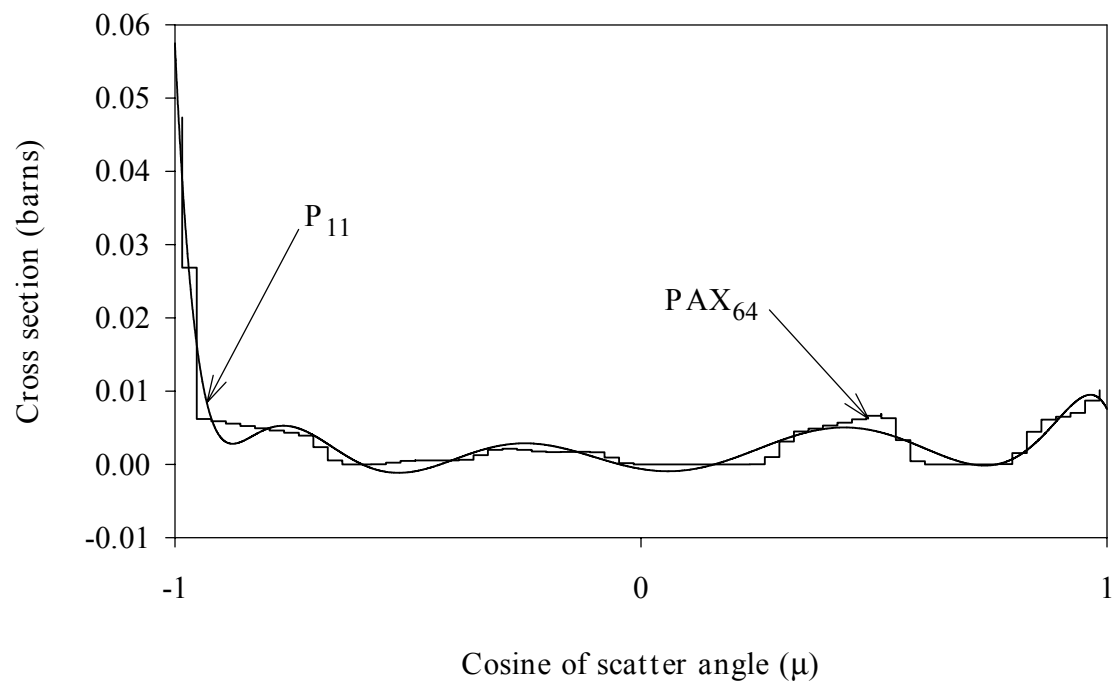
Figure 4: ^{10}B cross section for group 1 to 15 in 117-group structure
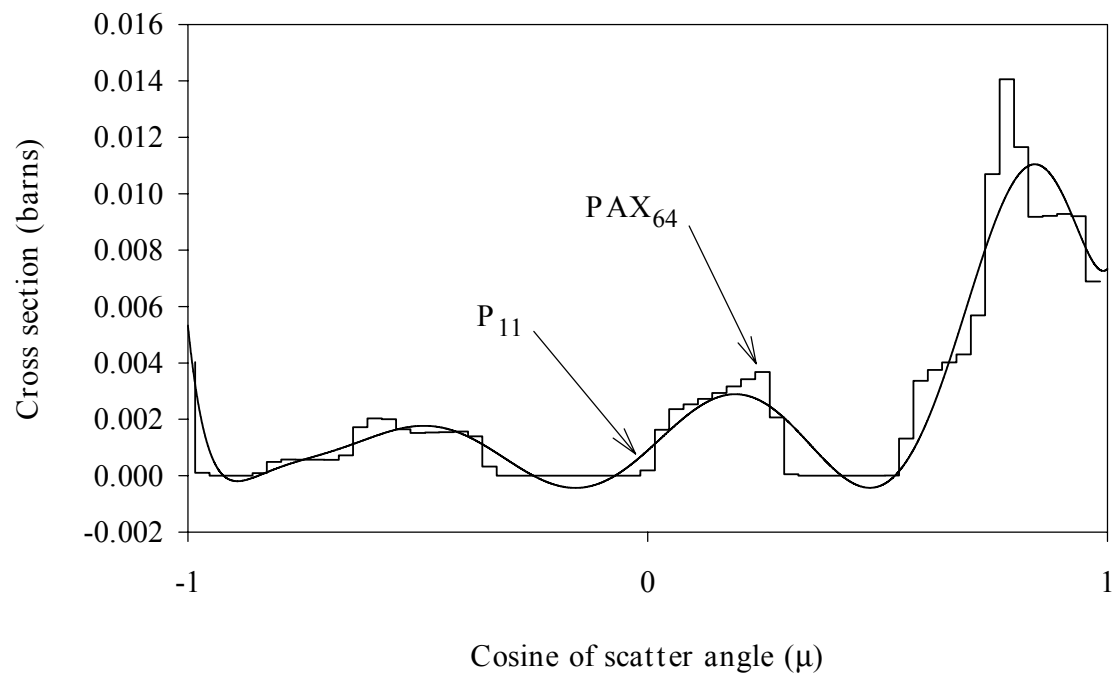
Figure 5: ^{10}B cross section for group 1 to 16 in 117-group structure
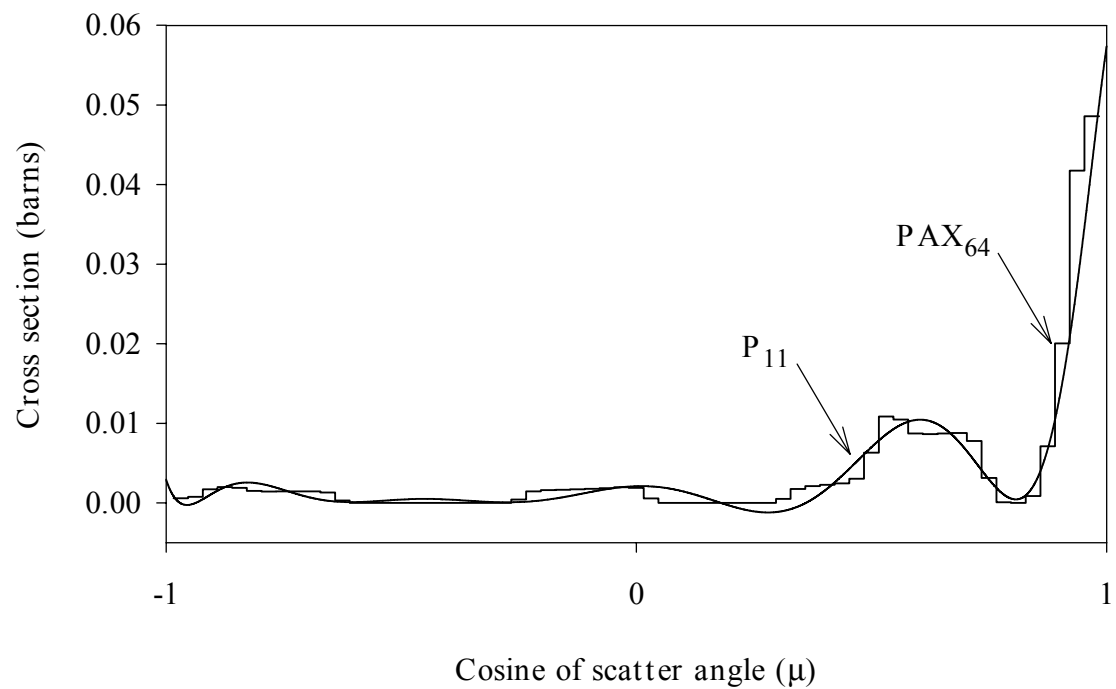
Figure 6: ^{10}B cross section for group 1 to 17 in 117-group structure

The truncated Legendre expansions may perform adequately for the occasional combination of material, Legendre order, and energy group structure. But changing

any one of these contributors to a previously adequate combination, for example the energy group in the figures above, can lead to regions of negativity in the truncate Legendre expansion. Therefore, although the Legendre moments are efficient to generate and use for discretized transport, a truncated Legendre expansion does not guarantee the most important quality for transport data—non-negativity.

Another property of the group-to-group cross sections is discontinuities in the first derivative. And consequently, the globally smooth truncated Legendre expansions do not converge uniformly. This point-wise convergence of the truncated Legendre expansion is another disadvantage of the approximation because increasing the number of moments included in the expansion to recover the group-to-group cross sections does not guarantee a more accurate solution throughout the entire domain of the expansion.

When the two approximations, discrete ordinates and a truncated Legendre expansion for the cross section, are combined, several artifacts are obscured. Additionally, the combination of the two approximations, neither of which converges uniformly, leads to a certain art whereby the order of the Legendre truncation and the number of ordinates to use is divined through experience.

The lack of angular support in the discrete ordinates is obscured because the truncated Legendre expansion is non-zero for all points between -1 and 1 except for the finite number of nodes. The combined approximation will have both negative cross sections for certain directions and positive cross sections for other directions where the group-to-group cross section would be zero. Thus, the lack of angular support is obscured.

Combining truncated Legendre expansions and discrete ordinates angular quadratures can lead to negative scalar fluxes in two ways. Using the equation to calculate the scalar flux

$$f_g = \sum_{n=1}^{N} w_n y_{n,g}, \tag{12}$$

having either negative weights, w_n, or negative angular fluxes can lead to negative scalar fluxes. The negative angular fluxes can arise from having a discrete ordinates quadrature set with an angle between two ordinates that falls in a region of negativity in the truncated Legendre expansion for the group-to-group scatter cross section. This ordinate-to-ordinate pair with a negative value for the scatter cross section can lead to a

negative scatter source. If no other source is present in the spatial cell, then the angular flux solution will be negative. Having an angular quadrature set with negative weights (although this is always avoided in practice) could also lead to negative scalar fluxes. Therefore, I reject discrete ordinates with truncated Legendre expansions for the cross section because the two important properties of the BTE can be lost using this combination of approximations—non-negative fluxes and non-negative input data.

II.2: Evaluation of Bin-to-Bin Cross Sections by Multidimensional Monte Carlo Numerical Integration

DelGrande and Mathews (7) used Monte Carlo numerical integration to generate the bin-to-bin cross sections. This bin-to-bin cross section, restated from chapter 1, is

$$
s_{n'n,g'g} = \frac{\displaystyle\int_{\Delta W_{n'}} dW' \int_{\Delta W_n} dW \int_{\Delta E_{g'}} dE' \int_{\Delta E_g} dE\, s^s\left(E' \rightarrow E, \hat{W}' \times \hat{W}\right) F(E')}{\Delta W_{n'} \displaystyle\int_{\Delta E_{g'}} dE'\, F(E')}.
$$
(13)

This integral is slow to converge with Monte Carlo and the stochastic convergence does not guarantee that all possible bin-to-bin scatters are taken into account without using an infinite number of samples. And, of the bin-to-bin scatters that are taken into account, many bin-to-bin pairs will have large stochastic errors due to the slow convergence of Monte Carlo integration. In practice, DelGrande and Mathews (7) assumed that scatters with low probability, and consequently large stochastic error, would not contribute significantly to the transport result. Scatters with low probability can be the dominant source of particles at some energies in some locations of some transport problems. I present an example of this in a shield penetration problem in chapter 6. I reject the Monte Carlo evaluation of the bin-to-bin cross section because of its slow convergence and large stochastic error.

To reduce the stochastic error and improve efficiency and accuracy, variance reduction techniques were investigated for use in the Monte Carlo evaluation of the bin-to-bin cross section. As the various ENDF/B-VI scatter mechanisms were investigated, several of the integrations had either analytic solutions or could be deterministically integrated. The replacement of the Monte Carlo integrations using deterministic

quadratures or analytic integrations continued following the textbook on variance reduction for Monte Carlo by Hammersley,

> It should almost go without saying, if it were not so important to stress it, that whenever in the Monte Carlo estimate of a multiple integral we are able to perform part of the integration by analytical means, that part should be so performed. As in some other kinds of gambling, it pays to make use of one's knowledge of form. (9)

Eventually, it was determined that all of the nested integrations in equation (13) could be integrated either deterministically or analytically. The Monte Carlo quadrature used by DelGrande and Mathews (7) was abandoned, leading to the methods used in section II.4.

II.3: SCATTER CROSS SECTION OPERATOR

The two methods, bin-to-bin cross section evaluation with Monte Carlo integration and truncated Legendre expansions for cross section, can be combined and extended using the scatter cross section operator that I define as

$$S_{g'g}[g] \equiv \frac{\int_{-1}^{1} d\mu \int_{\Delta E_{g'}} dE' \int_{\Delta E_g} dE\, \sigma^s(E'\rightarrow E, \mu)\Phi(E')g}{\int_{\Delta E_{g'}} dE'\, \Phi(E')}, \tag{14}$$

where g is any real function of μ defined everywhere in the interval $[-1,1]$. $S_{g'g}$ is a mapping from the function space which comprises its domain to the real line. It is a linear functional as defined by Stakgold (20).

$$h_{n'n}(\mu) = \frac{\int_{\Delta\Omega_{n'}} d\Omega' \int_{\Delta\Omega_n} d\Omega\, \delta\left(\mu - \hat{\Omega}'\cdot\hat{\Omega}\right)}{\Delta\Omega_{n'}} \tag{15}$$

is the conditional probability that a particle, uniformly distributed in $\Delta\Omega_{n'}$ will scatter into $\Delta\Omega_n$ given that it does scatter and that the cosine of the angle of that scatter is μ. Because this conditional probability is entirely determined by the choice of a partition of the unit sphere into elements of solid angle, $\Delta\Omega_n$, ie. by the discrete elements angular quadrature set, $h_{n'n}(\mu)$ can be pre-computed and tabulated.

The element-to-element conditional probability function has been numerically evaluated and tabulated using a Monte Carlo numerical integration. It has also been numerically evaluated using a Gauss-Chebyshev numerical quadrature for the special case of one-dimensional transport (14).

The scatter cross section operator acting on the function $h_{n'n}(m)$ is

$$S_{g'g} h_{n'n}(m) = \frac{\int_{-1}^{1} dm \int_{\Delta E_{g'}} dE' \int_{\Delta E_{g'}} dE\, \sigma^s(E'\to E, m) F(E') \int_{\Delta\Omega_{n'}} d\Omega' \int_{\Delta\Omega_n} d\Omega\, \delta(m - \hat\Omega'\times\hat\Omega)}{\int_{\Delta\Omega_{n'}} d\Omega' \int_{\Delta E_{g'}} dE'\, F(E')}. \tag{16}$$

Rearranging the integrals and performing the integration over the delta distribution function introduced in equation (15) gives the equation

$$S_{g'g} h_{n'n}(m) = \frac{\int_{\Delta\Omega_{n'}} d\Omega' \int_{\Delta\Omega_n} d\Omega \int_{\Delta E_{g'}} dE' \int_{\Delta E_g} dE\, \sigma^s(E'\to E, \hat\Omega'\times\hat\Omega) F(E')}{\Delta\Omega_{n'} \int_{\Delta E_{g'}} dE'\, F(E')}. \tag{17}$$

The bin-to-bin cross section is therefore

$$\sigma_{n'n,g'g} = S_{g'g} h_{n'n}. \tag{18}$$

The Legendre moments for the truncated Legendre expansion of the scatter cross section can be obtained by operating on $P_l(m)$ with S:

$$\sigma_{l,g'g} = S_{g'g} P_l(m) = \frac{\int_{-1}^{1} dm \int_{\Delta E_{g'}} dE' \int_{\Delta E_{g'}} dE\, \sigma^s(E'\to E, m) F(E') P_l(m)}{\int_{\Delta E_{g'}} dE'\, F(E')}, \tag{19}$$

which is the equation for generating the Legendre moments of the scatter cross section.

Piecewise-average group-to-group scatter cross sections (PAX) can be obtained using the scatter cross section operator:

$$\bar\sigma_{g'g,k} = S_{g',g} \frac{H(m - m_{k-1}) H(m_k - m)}{\Delta m_k}. \tag{20}$$

15

where H is the Heaviside function, $k = 0 \text{K } K$, and

$$m_k = -1 + \frac{2k}{K}. \tag{21}$$

PAX cross sections have several advantages compared to either truncated Legendre moments or Monte Carlo evaluation of bin-to-bin cross sections. They are non-negative and converge uniformly. The PAX cross sections can be used for discrete elements, discrete ordinates, or multi-group Monte Carlo transport having been calculated once for given: material, energy group structure, $F(E\phi)$, number of pieces, and temperature. In the remaining chapters, I have developed, validated, and demonstrated an algorithm to calculate the PAX cross sections using deterministic quadratures for the integrations in equation (20). My algorithms use deterministic quadratures to control the quadrature error introduced in approximating equation (20). PAX cross sections are accurate for each group-to-group pair because each mechanism represented in ENDF/B-VI and each group-to-group pair are calculated independently.

II.4: APPLICATIONS OF PIECEWISE-AVERAGE GROUP-TO-GROUP SCATTER CROSS SECTIONS

II.4.1: Bin-to-Bin Cross Sections

PAX cross sections can be used in a very efficient way to approximate the bin-to-bin cross sections:

$$s_{n\phi n,g\phi g} \approx \sum_{k=1}^{K} h_{n\phi n,k} \bar{s}_{g\phi g,k}, \tag{22}$$

where

$$h_{n\phi n,k} = \int_{m_{k-1}}^{m_k} dm\, h_{n\phi n}(m) \tag{23}$$

If the piecewise conditional scattering probabilities $h_{n\phi n,k}$ are pre-computed and stored for a particular discrete elements angular quadrature set and choice of K, and similarly, the PAX cross sections $\bar{s}_{g\phi g,k}$ are pre-computed and stored, then the set of $s_{n\phi n,g\phi g}$ values is obtained by the simple tensor contraction in equation (22) with no redundant calculations.

16

II.4.2: Legendre Moments

Likewise, a numerical approximation to the Legendre moments of the scatter cross section in equation (19) using the PAX cross section is

$$s_{l,g \xcancel{g}} \approx \sum_{k=1}^{K} \frac{(2l+1)}{2} P_{l,k} \, \bar{s}_{g \xcancel{g},k}, \tag{24}$$

where

$$P_{l,k} = \int_{m_{k-1}}^{m_k} dm P_l(m) \tag{25}$$

Computational efficiency like that for the bin-to-bin cross sections is achieved for the Legendre moments by pre-computing and storing an array of $\frac{(2l+1)}{2} P_{l,k}$ for $l = 0\mathrm{K}\,L$ and $k = 1\mathrm{K}\,K$, for a choice of L and K.

II.4.3: Multi-Group Monte Carlo Transport

In addition to the fully discretized transport methods, multi-group Monte Carlo transport could also use the PAX cross sections by creating a tabular cumulative distribution function to invert by table search and interpolation. The conventional method for generating group-to-group cross sections for multi-group Monte Carlo creates a strictly positive representation of the scatter cross section from a truncated Legendre expansion using a maximum entropy method (5, 11). Sixteen equally-likely intervals of m are then created from this strictly positive representation. As shown in Figure 1, however, the group-to-group cross sections can have several separated regions of zero value. Neither the 16 equal-likelihood intervals nor the strictly positive maximum entropy method accurately approximates these zero-value regions. Therefore, I expect the PAX cross sections would be more accurate than the conventional method for creating group-to-group Monte Carlo cross sections (although this research is left for a future effort).

II.5: FAILURE OF POINT-WISE EVALUATION OF THE GROUP-TO-GROUP CROSS SECTIONS

The PAX cross sections are a finite volume approach rather than a numerical quadrature based on interpolation between point values, such as composite midpoint:

$$\sigma_{n'n,g'g} \approx \sum_{k=1}^{K} h_{n'n}\left(\frac{\mu_{k-1}+\mu_k}{2}\right)\sigma_{g'g}\left(\frac{\mu_{k-1}+\mu_k}{2}\right),\tag{26}$$

where

$$\sigma_{g'g}(\mu_k)=\int_{\Delta E_{g'}} dE'\int_{\Delta E_g} dE\,\sigma(E'\rightarrow E,\mu_k)F(E').\tag{27}$$

An attempt was made to evaluate the group-to-group cross sections at a grid of points for use within a numerical quadrature based on interpolation. Point-wise evaluation of the group-to-group cross section fails due to poles in $\sigma_{g',g}^{mech}(\mu_L)$ for the level inelastic scatter mechanism (where μ_L is the cosine of the scatter angle in the laboratory frame of reference). The level inelastic scatter mechanism can have an ENDF/B-VI representation in the center of mass frame of reference. Evaluating the cross section in the laboratory frame (the frame of the transport problem) involves transforming the distribution function for the cosine of the scatter angle into the laboratory frame using

$$f(\mu_L)=f(\mu_{CM})\left|\frac{d\mu_{CM}}{d\mu_L}\right|,\tag{28}$$

where f represents the distribution function for the special case of the angular distribution described in section III.1.4, and μ_{CM} is the cosine of the scattering angle in the center of mass frame of reference. For the level inelastic scattering mechanism, this transformation is infinite as μ_L approaches 1 and the incident energy of the neutron approaches the energy deficit. The result is that the incident energy integration in equation (26) fails to converge.

Numerically evaluating the PAX cross sections

$$\sigma_{g'g,k}=\int_{-1}^{1}\mu^{CM}\int_{\Delta E_{g'}} dE'\int_{\Delta E_g} dE\,\sigma(E'\rightarrow E,\mu^{CM})F(E')*$$

$$\left[\frac{H\left(\mu^L(\mu^{CM})-\mu_{k-1}\right)H\left(\mu_k-\mu^L(\mu^{CM})\right)}{\Delta\mu_k}\right]\tag{29}$$

is not a problem because $s\left(E \not\circledR\ E, m^{CM}\right)$ is well-behaved, and $\left|\dfrac{dm_{CM}}{dm_L}\right|$ does not

appear because H is a point function, not a distribution function.

III. Implementation

The numerical approximations to the group-to-group scatter cross sections using the scatter cross section operator defined in chapter 2 have been implemented in a computer code. This computer code uses ENDF/B-VI data to generate the three different numerical approximations using the scatter cross section operator. Although a computer code could have been written to implement only the new PAX cross sections, I decided to implement a single code that could perform all three different group-to-group cross section approximations: Legendre moments, bin-to-bin cross sections, and PAX cross sections, because the new PAX cross sections would have to be validated against existing codes that only output either bin-to-bin cross sections or Legendre moments.

My code philosophy balances efficiency, robustness, and code readability. The programming language FORTRAN 90/95 has self-documenting features such as extended variable names and modular structure. Coding decisions were made to emphasize readability for the purpose of debugging. Therefore, the improvements in efficiency in the computation are a consequence of the algorithms discussed in this chapter and the cross section operator discussed in chapter 2. Code optimization is left to the compiler.

This chapter presents several algorithms used in the new computer code. These algorithms use some FORTRAN 90/95 key words. These key words are summarized in appendix B, and are printed in an italic, mono-spaced font, e.g. *ElseIf*.

ENDF/B-VI data is used directly so that no intermediate approximations are used prior to calculating the group-to-group cross sections. DelGrande and Mathews (7) used an intermediate output from the NJOY code called A Compact ENDF (ACE) file (13). The NJOY code uses approximations to generate the ACE files. These approximations introduce errors that cannot be controlled by the user of the new computer code. NJOY has its own residual constraints from earlier assumptions about computational power and resources because it was developed during the 1970s.

III.1: Cases for Secondary Energy and Angular Distributions

In general, ENDF/B-VI represents scatter cross sections as

$$\sigma^s(E' \rightarrow E, \mu) = \sigma(E')n(E')f_{joint}(\mu, E \,|\, E'), \tag{30}$$

where the joint distribution is normalized as

$$\int dE \int d\mu\, f_{joint}(\mu, E \,|\, E') = 1, \tag{31}$$

and the multiplicity function, $n(E')$, represents the number of secondary neutrons created as a function of the incident energy. The multiplicity function is often used for fissionable isotopes but can also be used to represent the number of secondary neutrons in reactions such as (n, 2n). With the inclusion of the multiplicity function in the scatter cross section by ENDF/B-VI, the fission cross section is a mechanism to be used within the scatter cross section operator.

The joint distribution can be expressed in three ways,

$$f_{joint}(\mu, E \,|\, E') = \begin{cases} f(\mu | E, E')g(E \,|\, E') \\ g(E \,|\, E')f(\mu | E', E) \\ f(\mu | E', E)g(E \,|\, E', \mu) \end{cases} \tag{32}$$

Each of these three cases, have approximations of f and g, and those approximations are called laws by ENDF/B-VI notation. Elastic and level-inelastic scatter are treated together as a special case.

All three of these cases can be represented in ENDF/B-VI in either the center of mass reference frame or the laboratory reference frame. If the ENDF/B-VI data is represented in the center of mass reference frame, then the scatter cross section operator is transformed from the laboratory reference frame to the center of mass reference frame. Otherwise, if the ENDF/B-VI data is represented in the laboratory reference frame, then the scatter cross section operator is not transformed.

The cross section function, $\sigma(E')$, may be quite smooth over large energy ranges or it can vary rapidly in regions where resonances are present for a given material. The rapidly varying resonance regions are represented using parameterized functions with tabulated parameters. Other regions are represented by interpolation functions using tabulated values.

The scatter cross section operator is restated for convenience with the above approximation of the continuous scatter cross section from ENDF/B-VI as

$$S_{g'g} = \frac{\int_{\Delta E_{g'}} dE'\, s(E')\, n(E')\, F(E') \left\{ \int_{\Delta E_g} dE \left[\int_{-1}^{1} dm\, f_{joint}(m, E\,|\,E') \right] \right\}}{\int_{\Delta E_{g'}} dE'\, F(E')}. \qquad (33)$$

The explicit nesting of the integrals in the scatter cross section operator is used to show the different dependencies of the cases.

Three cases for the joint distribution are presented. Then, elastic and level inelastic scatter are presented as an important special case. The mechanisms that typically use each of the cases are presented. The actual ENDF/B-VI laws are stated in appendix F.

III.1.1: Separable Energy and Angular Distributions

The assumption in the first case is the separability of the secondary energy distribution and the scatter angle distribution. It is

$$f_{joint}(m, E\,|\,E') = f(m\,|\,E')\, g(E\,|\,E'). \qquad (34)$$

This distribution is often used for representations such as fission or (n, 2n) reactions. This representation is only chosen when the reactions produce at least three secondary particles, ie. two neutrons and a remaining nucleus. This three-body problem results in a weak dependence between the angular distribution and the secondary energy distribution of the secondary particles. The ENDF/B-VI evaluators can then reasonably separate the joint distribution into two separate distributions.

With separable energy and angular distributions, the integrals in the scatter cross section operator can be rearranged as

$$S_{g'g} = \frac{\int_{\Delta E_{g'}} dE'\, s(E')\, n(E')\, F(E') \left[\int_{-1}^{1} dm\, f(m\,|\,E') \right] \left\{ \int_{\Delta E_g} dE\, g(E\,|\,E') \right\}}{\int_{\Delta E_{g'}} dE'\, F(E')}. \qquad (35)$$

Calculating a mechanism with a separable energy and angular distribution is the most efficient case because the integration requires only two-level nesting of

quadratures. Section III.4.1 presents the algorithm I use to calculate the two innermost integrations.

III.1.2: Angular Distribution Dependent on Secondary Energy

The second case has an angular distribution dependent on the secondary energy. This case is

$$f_{joint}\left(m, E \mid E'\right) = g\left(E \mid E'\right)f\left(m \mid E' \to E\right). \tag{36}$$

This case can be used for any (n, n+product) reactions, where the product can be a neutron, multiple neutrons, a proton, an alpha particle, etc. It is used when the secondary energy and the angular distribution are more strongly correlated. It can also be used when the ENDF/B-VI evaluators have so little information that only a rough assumption about the secondary energy and angular distributions can be made. The rough approximation to the angular and energy correlation may be due to the large number of products produced during the reaction. For both possibilities, the second case can represent the appropriate ENDF/B-VI laws. The integrals in the scatter cross section operator can be rearranged as

$$S_{g'g} = \frac{\int_{\Delta E_{g'}} dE' s\left(E'\right) n\left(E'\right) F\left(E'\right) \left\{ \int_{\Delta E_g} dE \left[g\left(E \mid E'\right) \int_{-1}^{1} dm f\left(m \mid E' \to E\right) \right] \right\}}{\int_{\Delta E_{g'}} dE' F\left(E'\right)}. \tag{37}$$

This case takes the most computational time due to the three-level nesting of the quadrature.

III.1.3: Secondary Energy Distribution Dependent on Scatter Angle

The last case is used for only one law in ENDF/B-VI: the laboratory angle-energy law. This case is

$$f_{joint}\left(m, E \mid E'\right) = f\left(m \mid E'\right) g\left(E \mid E' \to m\right). \tag{38}$$

In rare circumstances, the ENDF/B-VI evaluators can only accurately determine the secondary energy of the products of the reaction as a function of angle, as in a laboratory experiment. Then, the secondary energy distribution is clearly dependent on the scatter angle and this appropriate law is chosen.

The use of the laboratory angle-energy law in ENDF/B-VI is so rare that I did not find an example that used it. Nevertheless, my code does support this option by rearranging the integrals in the scatter cross section operator as

$$S_{g'g} = \frac{\int_{\Delta E_{g'}} dE'\, s\,(E')n\,(E')F\,(E')\int_{-1}^{1} d\mu \left\{ f\,(\mu|E')g\int_{\Delta E_{g'}} dE\, g\,(E\,|E',\mu) \right\}}{\int_{\Delta E_{g'}} dE'\, F\,(E')}. \tag{39}$$

Presumably, this is also computationally expensive because of the three-level nesting of the quadrature.

III.1.4: Elastic and Level Inelastic Scatter Cases

The special case for the third case is elastic and level inelastic scatter mechanisms. In these mechanisms, the secondary energy of the neutron is uniquely determined by the incident energy and the angle of scatter, with the formula

$$f_{joint}\,(\mu, E\,|E') = f\,(\mu|E')\delta\,(E - E_s\,(E',\mu)), \tag{40}$$

where E_s is determined by conservation of energy and momentum as

$$E_s\,(E',\mu) = \frac{1}{(A+1)^2}\left[\mu\sqrt{E'} \pm \sqrt{E'\,(\mu^2 + A^2 - 1) + A\,(A+1)Q}\right]^2, \tag{41}$$

and where Q is "the *excess* of kinetic energy of the product particles over that of the original particles" (11), and A is the ratio of the mass of the target nucleus to the mass of the neutron.

The integrals in the scatter cross section operator can be rearranged as

$$S_{g'g} = \frac{\int_{\Delta E_{g'}} dE'\, s\,(E')n\,(E')F\,(E')\int_{\mu'\,E_g \le E \le E_{g-1}} d\mu f\,(\mu|E',\Delta E_g)g}{\int_{\Delta E_{g'}} dE'\, F\,(E')}, \tag{42}$$

where the secondary energy group boundaries, E_g and E_{g-1}, are included in the bounds of the integration with respect to μ. The bounds can be obtained from equation (41) given E', E, and Q.

The special case of elastic and level inelastic scatter is the most frequently used and typically contributes the most to the group-to-group scatter cross sections. Although finding the limits of integration of the cosine of the scattering angle takes extra computational time, the overall computational effort is comparable to the first case (section III.1.1) of separable energy and angular distributions. Additionally, because the neutron can always scatter elastically at any incident energy, this special case is always used for each incident energy group.

III.2: QUADRATURES

Two adaptive quadratures, Simpson and Gauss-Simpson, were used to perform the needed nested integrations. Both adaptive quadratures used FORTRAN 90/95 recursion to subdivide intervals as necessary to achieve user-set error tolerances. Two other quadrature methods were also considered, but were discarded—Romberg integration (4) and IMSL (5) adaptive integration routines.

III.2.1: Characteristics of the Integrand

Section III.1 presented four cases of nested integrations. Each of the nested integrations uses data from ENDF/B-VI. The data from ENDF/B-VI is associated with laws that describe the use of either tabulated data or tabulated parameters for reconstruction of the data. For either type of ENDF/B-VI data, the characteristics of the integrands in section III.1 are similar:

1. Finite number of discontinuities in the integrand
2. Finite number of discontinuities in the first derivative of the integrand
3. Localized, non-polynomial behavior
4. Finely partitioned domain to handle the characteristics in #1 and #2 above

A quadrature with a robust, adequate, and practical implementation was needed to address the characteristics of the integrand. The discontinuities in the integrand and the first derivative of the integrand require a relatively fine initial mesh for any of the integrations described in section III.1. With a relatively fine initial mesh, a modest order numerical quadrature is sufficient. The localized, non-polynomial behavior requires an adaptive method. An open quadrature method does not evaluate the integrand at the endpoints of the domain, but a closed quadrature method uses at least the endpoints of the domain of integration. And, to avoid data and code complexity to

use only a closed method, both open and closed methods were used when appropriate. An algorithm of modest order, adaptive, and with either open or closed methods addressed each of the characteristics of the integrand.

III.2.2: Romberg Integration

The first numerical quadrature discarded was a Romberg automatic integration, given in numerical methods texts such as Burden and Faires (4). The Romberg numerical method was discarded for two reasons, global error testing and closed end-point method. The Romberg method uses a global convergence test. I used the relative error

$$e_{rel}(x,y) = \frac{|x - y|}{(|x| + |y|)/2}.$$

(43)

If the entire integration did not pass the relative error tolerance, then another Romberg iteration was performed. Because each Romberg iteration is twice as expensive as the previous iteration, this method was slower to converge than the adaptive quadrature methods used. In practice, the global error in the integration could be dominated by only one or two sub-domain pieces. Despite this, Romberg subdivides all the subintervals.

Romberg integration is a succession of composite trapezoid quadratures with an Aitken extrapolation for the next approximation to the integral. The trapezoid numerical quadrature is a closed quadrature, which is not useful for several of the nested quadratures required in evaluating the integrals in section III.1. One could use a Romberg scheme based on composite midpoint, which is an open rule, but it is even less efficient. In order to reuse function evaluations, it requires 3^n evaluations for n levels of subdivision; composite trapezoid requires only 2^n.

III.2.3: IMSL Adaptive Integration Routines

IMSL's adaptive quadratures (5) were not used for two reasons. The first reason is that they use Gauss-Kronrod quadrature in each subinterval; thus the number of points used was excessive—17 points in each subinterval. Usually, the partitioning of the domain to account for discontinuities was sufficient for the relative error tolerance to be passed with a far more modest number of points, such as those used in either Simpson or Gauss-Simpson adaptive methods.

26

The second reason that the IMSL routines were not used is the many required different subroutines and variations. The IMSL integration routines are written in FORTRAN 77 and pre-compiled, and consequently are not recursive. Without recursion, the same IMSL library routine cannot be used for nested integrals. Therefore, the IMSL routines were discarded due to a lack of flexibility and excessive number of quadrature points.

III.2.4: Adaptive Simpson Integration

The limits of integration and the integrand are assumed to be separate subroutines to either adaptive integration quadrature. Given the limits of integration, any places in the domain where the integrand is discontinuous or its first derivative is discontinuous must be found and tabulated. The initial tabulation is used as a mesh for the adaptive quadratures. The adaptive quadratures then integrate each of the mesh pieces individually. Each of the adaptive methods performs two quadratures on the subinterval. If the two quadratures pass a relative error test for convergence, then the integration on the subinterval is complete; otherwise, the subinterval is subdivided and each sub-piece is integrated and tested for convergence individually.

The adaptive Simpson routine (Algorithm 1) is logically correct. In the code, it is implemented with additional arguments in order to avoid redundant function evaluations and quadrature calculations. The algorithm for the adaptive Simpson method is covered first because the adaptive Simpson method is embedded in the adaptive Gauss-Simpson method.

Algorithm 1: Adaptive Simpson

   Input: x_0, x_1
   Output: Q
   $Dx = x_1 - x_0$

$$Q_0 = \left(f(x_0) + 4f(x_0 + Dx/2) + f(x_1)\right)Dx/3$$

$$Q_L = \left(f(x_0) + 4f(x_0 + Dx/4) + f(x_0 + 1/2Dx)\right)Dx/6$$

$$Q_R = \left(f(x_0 + Dx/2) + 4f(x_0 + 3Dx/4) + f(x_1)\right)Dx/6$$

$$Q_1 = Q_R + Q_L$$

   $If\ (\ 2|Q_1 - Q_0| \pounds\ e_{rel}(Q_1 + Q_0)\ )\ Then$

$$Q = Q_1$$

```
Else
```
Left integral = Adaptive Simpson $(x_0, x_0 + \dfrac{x_0 + x_1}{2})$

Right integral = Adaptive Simpson $(x_0 + \dfrac{x_0 + x_1}{2}, x_1)$

Q = Left integral + right integral
```
End If
```

III.2.5: Adaptive Gauss-Simpson Integration

The adaptive Gauss-Simpson initially uses a two point Gauss-Legendre quadrature. If the relative error tolerance is not passed, then the Gauss subroutine calls two different Gauss-Simpson subroutines for each portion of the integrand.

Algorithm 2: Adaptive Gauss

Input: x_0, x_1

Output: Q

$h = \dfrac{x_1 - x_0}{2}$

$x_{mid} = \dfrac{x_0 + x_1}{2}$

$Q_0 = h \left(f \left(x_{mid} - \dfrac{h}{\sqrt{3}} \right) + f \left(x_{mid} + \dfrac{h}{\sqrt{3}} \right) \right)$

$h = \dfrac{h}{2}$

$x_{mid_1} = \dfrac{x_0 + x_{mid}}{2}$

$x_{mid_2} = \dfrac{x_{mid} + x_1}{2}$

$Q_L = h \left(f \left(x_{mid_1} - \dfrac{h}{\sqrt{3}} \right) + f \left(x_{mid_1} + \dfrac{h}{\sqrt{3}} \right) \right)$

$Q_L = h \left(f \left(x_{mid_2} - \dfrac{h}{\sqrt{3}} \right) + f \left(x_{mid_2} + \dfrac{h}{\sqrt{3}} \right) \right)$

$Q_1 = Q_R + Q_L$

```
If (2|Q_1 - Q_0| £ e_rel (Q_1 + Q_0) ) Then
    Q = Q_1
Else
```

28

Left integral = Adaptive Left Gauss-Simpson $(x_0, x_0 + \frac{x_0 + x_1}{2}, Q_L)$

Right integral = Adaptive Right Gauss-Simpson $(x_0 + \frac{x_0 + x_1}{2}, x_1, Q_R)$

Q = Left integral + right integral

`End If`

Algorithm 3: Adaptive Left Gauss-Simpson

Input: x_0, x_1, Q_{prev}

Output: Q

$h = \dfrac{x_1 - x_0}{4}$

$x_{mid} = \dfrac{x_0 + x_1}{2}$

$x_{mid_1} = \dfrac{x_0 + x_{mid}}{2}$

$Q_L = h\left(f\left(x_{mid_1} - \frac{h}{\sqrt{3}}\right) + f\left(x_{mid_1} + \frac{h}{\sqrt{3}}\right)\right)$

$Dx = x_1 - x_{mid}$

$Q_R = \left(f\left(x_{mid}\right) + 4f\left(x_{mid} + Dx/2\right) + f\left(x_1\right)\right)Dx/3$

$Q_1 = Q_R + Q_L$

`If (` $2|Q_1 - Q_0| \pounds\ e_{rel}(Q_1 + Q_0)$ `) Then`

$Q = Q_1$

`Else`

Left integral = Adaptive Left Gauss-Simpson $(x_0, x_0 + \frac{x_0 + x_1}{2}, Q_L)$

Right integral = Adaptive Simpson $(x_0 + \frac{x_0 + x_1}{2}, x_1)$

Q = Left integral + right integral

`End If`

Algorithm 4: Adaptive Right Gauss-Simpson

Input: x_0, x_1, Q_{prev}

Output: Q

$x_{mid} = \dfrac{x_0 + x_1}{2}$

$Dx = x_{mid} - x_0$

$Q_L = \left(f\left(x_0\right) + 4f\left(x_1 + Dx/2\right) + f\left(x_{mid}\right)\right)Dx/3$

$h = \dfrac{x_1 - x_0}{4}$

$$x_{mid_2} = \frac{x_{mid} + x_1}{2}$$

$$Q_R = h\left(f\left(x_{mid_2} - \frac{h}{\sqrt{3}}\right) + f\left(x_{mid_2} + \frac{h}{\sqrt{3}}\right)\right)$$

$$Q_1 = Q_R + Q_L$$

`If (` $2|Q_1 - Q_0| \le e_{rel}(Q_1 + Q_0)$ `) Then`

$$Q = Q_1$$

`Else`

    Left integral = Adaptive Simpson $(x_0, x_0 + \frac{x_0 + x_1}{2})$

    Right integral = Adaptive Right Gauss-Simpson $(x_0 + \frac{x_0 + x_1}{2}, x_1, Q_R)$

    Q = Left integral + right integral

`End If`

The adaptive Simpson integration is more efficient than the adaptive Gauss-Simpson because all of the points in the integration can be reused if additional subdivision is needed. This efficiency can improve the runtime of the calculation by approximately a factor of two.

The adaptive Gauss-Simpson integration method is used because it is an open rule. A two-point Gauss-Legendre quadrature method was used with composite Simpson because both methods have error $\mathcal{O}(Dx)^4$. Having more points in the Gauss-Legendre method would decrease efficiency because the points are discarded upon recursion.

III.3: MAIN PROGRAM AND INCIDENT ENERGY INTEGRATION

The portions of the algorithm that do not involve the scatter cross section operator reside in the main program. These include file input/output, looping through the incident energy groups, looping through the different mechanisms, and looping through the secondary energy groups. In the loop for the secondary energy group, a subroutine is called to perform the outer-most integral, the incident energy integral, for the scatter cross section operator for all four cases presented in section III.1

Algorithm 5: Main program

    `Call` GetENDFData
    Do g' = 1, G (number of energy groups)

```
Do mech = 1, M (number of mechanisms)
    If ( mechanism does not occur ) Cycle
    Call GetLimits( g_low, g_high )
    Do g = g_low, g_high
        Call IncidentEnergy( integral value(g, mech) )
    End Do
    Accumulate the sum of the integrals
End Do
Call OutputIntegral(g'-to-g integral )
End Do
```

Because the incident energy integration has no discontinuities in the integrand, it uses the recursive, adaptive Simpson method detailed in section III.2 for its efficiency. The incident energy mesh is constructed with special care because of the many places within the limits of integration for the incident energy group that its integrand, has, or could have, discontinuities in the first derivative. These discontinuities arise from the following places:

1. User-specified boundaries in the energy group structure

2. Tabulation of $s\left(E'\right)$ from ENDF

3. Tabulation of $n\left(E'\right)$ from ENDF

4. Tabulation of $F\left(E'\right)$ from user-set parameters

5. Tabulation of $f\left(m|E'\right)$ or $f\left(m|E'\to E\right)$ from ENDF

6. Discontinuous tabulation of either PAX cross sections or direct calculation of bin-to-bin cross sections with $h_{n'\to n}\left(m\right)$ when using elastic or level-inelastic scatter mechanisms because of implicit secondary energy group dependence

7. Tabulation of either $g\left(E\,|E'\right)$ or $g\left(E\,|E',m\right)$ from ENDF

Given an incident energy mesh with mesh points at all of the discontinuities in the first derivative, the algorithm for the incident energy mesh calls the recursive, adaptive Simpson method given in Algorithm 1 above for each mesh interval.

III.4: JOINT ANGULAR AND SECONDARY ENERGY DISTRIBUTION ALGORITHMS

The joint angular and secondary energy distributions use the three cases and the special case given in section III.1. The four cases use slightly different algorithms and I present them individually.

III.4.1: Separable Angular and Secondary Energy Distribution

The first case that is detailed in section III.1.1, separable angular and secondary energy distributions, uses two separate (as opposed to nested) integrations. The separable energy integration is performed using closed-form solutions for integrals of the functions using the tabulated parameters from ENDF/B-VI. The separable angular distribution is performed using the adaptive Gauss-Simpson method presented in section III.2 above. The PAX cross section, equation (20), has discontinuities in the cosine of the scatter angle mesh from the two Heaviside functions. Because I chose to include all of the different approximations for generating the group-to-group scatter cross sections from the cross section operator in one computer code, these discontinuities require use of the adaptive Gauss-Simpson method.

III.4.2: Angular Distribution Dependent on Secondary Energy

The second case presented in section III.1.2 has an angular distribution dependent on the secondary energy. This algorithm uses two nested, adaptive Gauss-Simpson calls. The secondary energy integration can have discontinuities in the tabulation for the secondary energy. Therefore, the open adaptive Gauss-Simpson method was an obvious choice. The integration for the angular distribution used the Gauss-Simpson method for the same reason as given in the separable case.

III.4.3: Secondary Energy Distribution Dependent on Scatter Angle

The third case presented in section III.1.3, in which the secondary energy distribution is dependent on the scatter angle, uses different integration methods for the outer and inner integrals. The outer integral, for the angular distribution, uses an adaptive Gauss-Simpson method as given in the separable case. The inner integral uses closed-form solutions for the integrations of the interpolating functions using the tabulated values of the secondary energy given by the ENDF/B-VI, laboratory angle-energy law.

III.4.4: Elastic and Level Inelastic Scatter

The elastic and level inelastic scatter special case described in section III.1.4 uses the adaptive Gauss-Simpson method for the same reason given in section III.4.1 for the separable angular distribution. There is no secondary energy group integration given in equation (42). To account for the secondary energy group, a subroutine to calculate the cosine of the scatter angle limits of integration dependent on the secondary energy group is added prior to the adaptive Gauss-Simpson integration.

To handle the laboratory frame transformation to the center of mass frame, an additional subroutine was required to transform the boundaries of the mesh used for the cosine of the scatter angle for either the PAX cross sections in equation (20) or for direct evaluation of the bin-to-bin cross sections in equation (17). A point-wise transformation was also required for the evaluation of the Legendre moments in equation (19). The same equation used for the transformation can be derived from equation (41) and is described in detail in the NJOY documentation (13).

III.5: DATA STRUCTURE

ENDF/B-VI allows cross-section evaluators to store data in any of numerous different ways. Compromises between memory requirements and efficiency in accessing the data within my code required some ingenuity and the use of FORTRAN 90/95 $allocatable$ arrays for dynamic memory usage.

These arrays are allocated at runtime to store the largest $extent$ of each of the dimensions needed for a mechanism's distribution. For example ^{10}B has several level inelastic scatter mechanisms available as well as an elastic scatter mechanism. Each of the mechanisms has potentially different data storage and representation. Therefore, I used $derived\ types$ to allow for all of the available choices for the angular distributions. This $derived\ type$ contains the integer flags necessary to identify the appropriate representation (one of the ENDF/B-VI laws listed in appendix F). Then, an array is allocated for each angular distribution representation to the largest $extent$ required by any of the mechanisms. Finally, the data is read from the input ENDF/B-VI file and filled into the appropriate representation array. One of the consequences of this approach is that the code must allocate extra integer arrays that contain the boundaries for each of the data arrays. To demonstrate how the arrays are

allocated and how the data is read into these arrays, a sample of a pseudo-code for one type of storage is provided in Algorithm 6.

Algorithm 6: Pseudo-code for reading and storing ENDF/B-VI data

```
Open ( ENDF file )
Do
    Read ( Character String, line number )
    If ( line number == exit line number ) Exit
End Do
Do
    Read ( mechanism number, ENDF law )
    If ( mechanism number /= valid mechanism number ) Cycle
    Select Case ( ENDF law )
    Case ( Legendre expansion )
        Read ( number of energy mesh, number of Legendre moments )
        max number energy mesh = Max ( new number, previous max )
        max number moments = Max ( new number, previous max )
    End Case
    Read ( next section number )
    If ( next section number /= this section number ) Exit
End Do
Close ( ENDF file )
Allocate ( energy data(max incident mesh) )
Allocate ( moment data(0:max number moments, max incident mesh) )
Open ( ENDF file )
Do
    Read ( mechanism number, ENDF law )
    If ( mechanism number /= valid mechanism number ) Cycle
    Select Case ( ENDF law )
    Case ( Legendre expansion )
        Read ( number of energy mesh, number of Legendre moments )
        Do i = 1, number of energy mesh
            Read ( energy data(i) )
            Read ( moment data(0:number of Legendre moments) )
        End Do
    End Case
    Read ( next section number )
    If ( next section number /= this section number ) Exit
End Do
```

IV. Cross Section Code Validation

I validated the cross section code by comparing its output with the results of two other codes: NJOY and DelGrande's Monte Carlo discrete elements cross section codes. Several online ENDF/B-VI plotting sites were also used for initial validation checks (19, 21). NJOY was used to validate the accurate evaluation of the secondary energy and angular distributions as well as the nested integrations. The online sites were used to directly validate the values produced by my code of the cross section data recreated from ENDF/B-VI. Comparing the new computer code to DelGrande's Monte Carlo discrete elements code validated the discrete elements approximation.

IV.1: DIRECT VALIDATION

Validation began by confirming that the input data had been read correctly from the ENDF/B-VI file. After checking the input, it was important to verify that the data was being faithfully represented and recreated. When dealing with the many different interpolation functions, ENDF/B-VI laws, and different reference frames, the faithful reconstruction of the cross section curves was essential.

Direct validation of the cross section curves involved examining and comparing many different plots for many different isotopes and mechanisms. The plots were then superimposed to determine whether or not the curves generated by my program matched those at respected online sites such as the ENDF/B-VI site (19) or the T2-Nuclear site (21), which is a site run by the group within the Los Alamos national laboratory that maintains and distributes the NJOY code.

All of the different resonance region parameterizations with Doppler broadening of the cross section and the tabulated cross sections were checked. The joint angular/secondary energy distributions were left to the NJOY validation portion. Figure 7 shows an example of one of the validations performed using the ENDF/B-VI site (19). The curve is the elastic scatter cross section of ^{56}Fe using the Reich-Moore resonance parameterization, which is one of the most complicated cross section curves represented in ENDF/B-VI files. To the limit of the benchmark data, this calculation is correct.
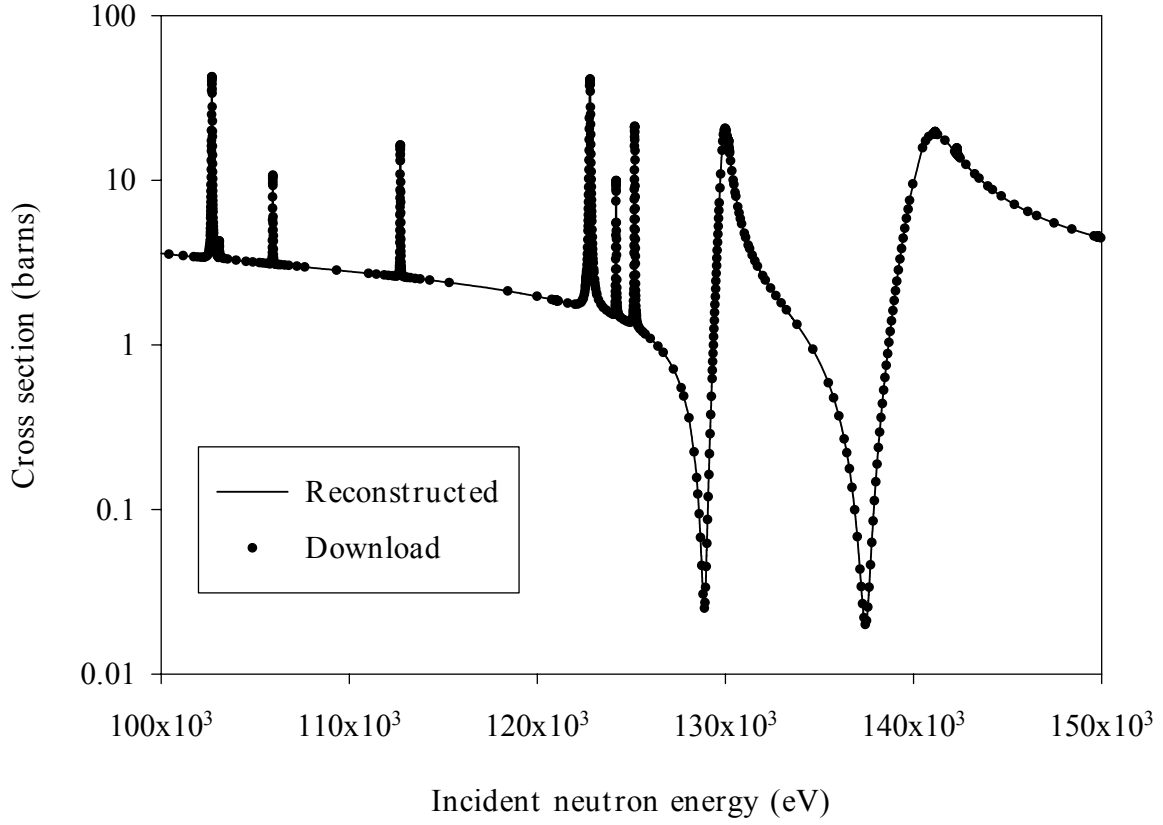
Figure 7: Comparison of download data to reconstructed data

^{56}Fe elastic scatter cross section reconstruction of Reich–Moore
resonance region parameterization broadened to 300K

IV.2: NJOY VALIDATION

Although the direct validation of the cross section curves is a powerful tool, it cannot validate everything in my new computer code. The validation of the reconstruction and integration of the angular and secondary energy distributions, as well as the integration of the cross section, used the NJOY code. Two methods using NJOY were employed—the development environment that contains a powerful debugging tool, and the output of the NJOY calculation.

IV.2.1: NJOY Validation Using the Development Environment

The Compaq Visual FORTRAN development environment (5) has two debugging features that I used for validation. Both debugging tools are used while performing step debugging, a runtime environment that allows a programmer to step

through the execution of a computer code line by line. The first feature allows the programmer to view the value of any variable while step debugging. The second feature allows the programmer to change the value of any variable during step debugging. Using these two tools, it was possible to enter a specific value for any of the different distributions in the new computer code. The calculated result of using the entered value could then be compared to the NJOY calculated result while both computer codes were running in a step debugging mode. Not only did this greatly aid the debugging of the new computer code; it also validated the new computer code when the two results matched within the single-precision NJOY uses for calculations. The interpolation of the tabulated data and other intermediate values were validated using these two tools.

IV.2.2: NJOY Validation Using Legendre Moments

The second validation method used the mechanism-specific Legendre moments output that is generated by NJOY. These NJOY Legendre moments could then be compared to two different computations of Legendre moments by the new computer code. The new computer code matched the Legendre moments from NJOY to the practical extent possible.

NJOY has several behaviors that make the comparisons difficult. The first NJOY behavior is the elimination of the output when the value of the cross section drops below 10^{-9} barns. This behavior creates a difficulty because some mechanism and group-to-group pairs have values below the NJOY cutoff. These could not be checked. Therefore, I was forced to rely upon the previous validations of the cross section curves and interpolations, and the validation of the group-to-group pairs above the cutoff.

Another behavior that makes comparison to NJOY difficult is limited error control within the program. For example, NJOY will perform some integrations using a pre-selected (hard coded) number of intervals for a composite quadrature. The code does not refine that mesh and compare quadrature results to test for convergence, nor does it use any other error control scheme. If the cross section involved is dominated by other mechanisms, this can be a practical approach, but it does not provide a reliable benchmark. In such cases, the NJOY result may only be good to one or two digits (out of the four digits printed).

The new computer code was designed to calculate and output the Legendre moments for comparison to the NJOY Legendre moments. The comparisons between NJOY and the direct calculations for the Legendre moments from my code were favorable and matched to within 0.1%. I considered this level of accuracy to validate the integration routines and the joint distributions that generate the Legendre moments. Table 1 presents a summary of an example isotope, mechanism, and energy group-to-group pair.

Validating the integration routines that generate the Legendre moments is a necessary condition for the PAX cross sections to be correct. But, I did not consider it sufficient. The approximation to the Legendre moments using PAX cross sections from equation (24) presented in chapter 2, were also generated and compared to the NJOY moments.

Method of Generation	0th moment	1st moment	2nd moment	3rd moment
NJOY	0.02432	-0.01391	0.002504	0.001285
New code using direct calculation	0.024317	-0.013913	0.0025041	0.0012850
New code with PAX_{64} approximation	0.024317	-0.013905	0.0024859	0.0013161

Table 1: Comparison of Legendre moments

^{10}B elastic scatter cross sections (in barns) for group 1 to 4 using LANL-30 defined in appendix D

All of the ENDF/B-VI representations were examined with results similar to this example. I consider the new computer code, including the new PAX cross section approximation, to have been successfully validated using the combination of the different comparisons.

IV.3: DISCRETE ELEMENTS VALIDATION

Although the PAX cross sections were validated by the investigation using NJOY, the PAX cross section used to generate bin-to-bin cross sections were also validated. I chose DelGrande's Monte Carlo cross section code (7) to use as a benchmark for bin-to-bin cross sections because it has been previously validated and published.

The element-to-element conditional probability, $h_{n \notin n}(m)$, was also validated directly by comparing the discrete quadrature one-dimensional code output to Monte Carlo estimates of $h_{n \notin n}(m)$ for all $(n \notin n)$ pairs of a slab-geometry DE$_8$ angular quadrature partition of the sphere (14). These agreed within the estimated uncertainties of the Monte Carlo calculations.

The approximation of the bin-to-bin cross sections using PAX cross sections presented in equation (22) agreed within the estimated uncertainties of DelGrande's Monte Carlo cross section code. I consider the bin-to-bin cross sections calculated using the PAX cross sections to be valid using the combination of the results from the NJOY comparison, the comparison to the DelGrande's Monte Carlo cross section code, and the direct comparison of the element-to-element conditional probability function to Monte Carlo calculations.

V. Performance of the PAX Cross Section Code

The performance scaling and the typical memory requirements for the PAX cross section portion of the scatter cross section code are presented. The code is examined to determine how the computer runtime scales with respect to: the number of energy groups, the number of tabulated PAX cross section points, and the desired accuracy of the calculation.

The runtime scaling power, p, can be empirically estimated from two computational runs with a parameter changing from N_1 to N_2 and runtimes Dt_1 and Dt_2

$$\left(\frac{N_2}{N_1}\right)^p = \frac{Dt_2}{Dt_1}, \tag{44}$$

hence,

$$p = \frac{Log\left(Dt_2/Dt_1\right)}{N_2/N_1}. \tag{45}$$

All of the examples in the following sections, with the exception of the investigated parameter, have been run with: the 30 group structure presented in appendix D, a material temperature of 300K, a relative error tolerance of 0.001, and a PAX mesh of 64 equal-width pieces. The computations were run on a computer with a 1 GHz processor and 512 MB of RAM. The examples are typical of other testing and evaluation performed.

V.1: SCALING WITH THE NUMBER OF ENERGY GROUPS

The runtime scales as approximately linear with the number of energy groups. As the number of groups increases from G_1 to G_2, the ratio of the non-zero group-to-group pairs, N_1^{pairs} to N_2^{pairs}, in the PAX cross section should vary as

$$\frac{N_2^{pairs}}{N_1^{pairs}} \mu \left(\frac{G_2}{G_1}\right)^2. \tag{46}$$

This does not result in quadratic scaling of the amount of computational effort because the amount of computation required for each group-to-group pair should be

proportional to DE_g, hence, inversely proportional to the number of energy groups, G.
The offset in the computational effort for each group-to-group pair combined with the
increase in the number of non-zero group-to-group pairs results in the observed
approximately-linear scaling

As an example, cross sections of the isotope ^{56}Fe were generated for 30, 59, and
117 groups using the new energy groups listed in appendix D. This isotope is
representative because it has a parameterized resonance region. Additionally, the ^{56}Fe
isotope has many different scatter mechanisms. Therefore, the runtime scaling is a good
average over many different effects.

Number of Groups	Computational Time	Scaling Power (p)
30	3246 seconds	
59	5193 seconds	0.69
117	10079 seconds	0.97

Figure 8: Scaling of code runtime with the number of energy groups

V.2: SCALING WITH THE NUMBER OF PAX CROSS SECTION PIECES

The scaling with the number PAX_K cross section pieces, or scaling with K, was
approximately quadratic. An increase in K linearly increases the computational cost of
the angular integration and also linearly increases the computational cost of the incident
energy integration. Nested, the two linear increases are quadratic scaling.

As an example, cross sections for ^1_1H were generated with K equal to 64, 128,
and 256. This isotope is a good example of runtime scaling as K increases because
elastic scatter is the only mechanism available and elastic scatter is present for all
materials and all incident energy groups.

Number of Points	Computational Time	Scaling Power (p)
64	6 seconds	
128	24 seconds	2.0
256	117 seconds	2.3

Figure 9: Scaling of the code runtime with PAX cross section pieces

V.3: IMPACT OF RELATIVE ERROR TOLERANCE ON RUNTIME

There is little increase in the runtime with lower relative tolerances. I investigated relative tolerances only as low as 0.0001 because the ENDF/B-VI data upon which the PAX cross sections depend are accurate to at most 4 digits. When the integrations are performed for the PAX cross sections, the relative error in the integrations usually met the tightest, 0.0001, relative tolerance. Therefore, relaxing the relative tolerance does not improve runtime drastically because often no extra recursion was required to pass the stricter tolerance.

As an example, cross sections of the isotope ^{56}Fe were generated with relative tolerance settings of 0.01, 0.001, and 0.0001.

Relative Error Tolerance	Computational Time
0.01	3014 seconds
0.001	3245 seconds
0.0001	4395 seconds

Figure 10: Runtime versus relative error tolerance

V.4: MEMORY REQUIREMENTS

The memory requirements for the PAX cross section code were quite modest. The most memory required for any of the materials and user-set input data was 40 MB of RAM. Typically, only 10 MB were needed. For practical work, the memory requirements are not limiting; the use of the dynamically allocated arrays presented in chapter 3 was successful.

VI. 1-D Transport Comparisons for Multi-Group Cross Section Approximations

This chapter presents two test problems to demonstrate the improvement of using the discrete elements approximation with PAX cross sections over the discrete ordinates approximation with truncated Legendre expansions for the group-to-group scatter cross sections. One-dimensional slab geometry transport favors the discrete ordinates approximation in comparison to the discrete elements approximation. The discrete ordinates Gauss-Legendre angular quadrature should approximate the angular flux solution better than the discrete elements composite midpoint rule because the solution for $y_g(x, m)$ is continuous in x and m, except at $m = 0$, given incident fluxes and emission sources that are continuous in m. Therefore, if discrete elements with PAX cross sections produces fluxes that are at least as good as those produced by discrete ordinates with truncated Legendre group-to-group scatter cross sections, then I anticipate that this will also be true in two- and three-dimensional transport, which favor the discrete elements approximation because $y_g(\vec{r}, \hat{W})$ need not be continuous in $\vec{r}$ and $\hat{W}$.

The two test problems use many of the same parameters for the cross sections and the transport.

1. Cross sections are Doppler broadened to 300 K.
2. 0.001 relative tolerance for piecewise average, group cross sections
3. 1.0×10^{-5} relative tolerance for transport convergence
4. PAX$_{64}$ cross sections
5. Symmetry boundary at left end
6. Vacuum boundary at right end
7. Energy-weight function, $F(E) = \frac{1}{E}$
8. Isotropic source in energy group 1 of the new 30, 59, and 117 group structures defined in appendix D

The source emits only in group 1 so that the computational artifacts of the anisotropic down-scatter into the lower energy groups would not be obscured by a source in those groups.

VI.1: TEST PROBLEM 1: THIN SOURCE EMBEDDED IN WATER

The first test problem has water throughout the entire problem with a symmetry boundary on the left and a vacuum boundary on the right. The source is located in a thin region of water on the left side of the problem emitting isotropically in energy group 1. The dimensions in the figure below are in centimeters.

Figure 11: Thin source embedded in water

Three energy groups out of the 30-group structure were chosen for comparison in this problem. The groups were chosen to demonstrate the differences between the anisotropic and isotropic computations as well as the differences between the discrete ordinates and discrete elements computations. Energy group 1 was chosen to show the impact of the anisotropy when the scalar flux solution is dominated by the removal cross section and streaming. Energy group 2 was chosen to show the impact of the anisotropy of the down-scatter source. Finally, energy group 28 was chosen to show that, although the anisotropy of the higher energy groups is important to the value of the cross section, the overall down-scatter source is mostly isotropic and both discrete ordinates and discrete elements perform well.

VI.1.1: Isotropic Comparison

The first series of figures compares calculations using both isotropic discrete ordinates (S_{12}/P_0) and isotropic discrete elements (DE_{12}).
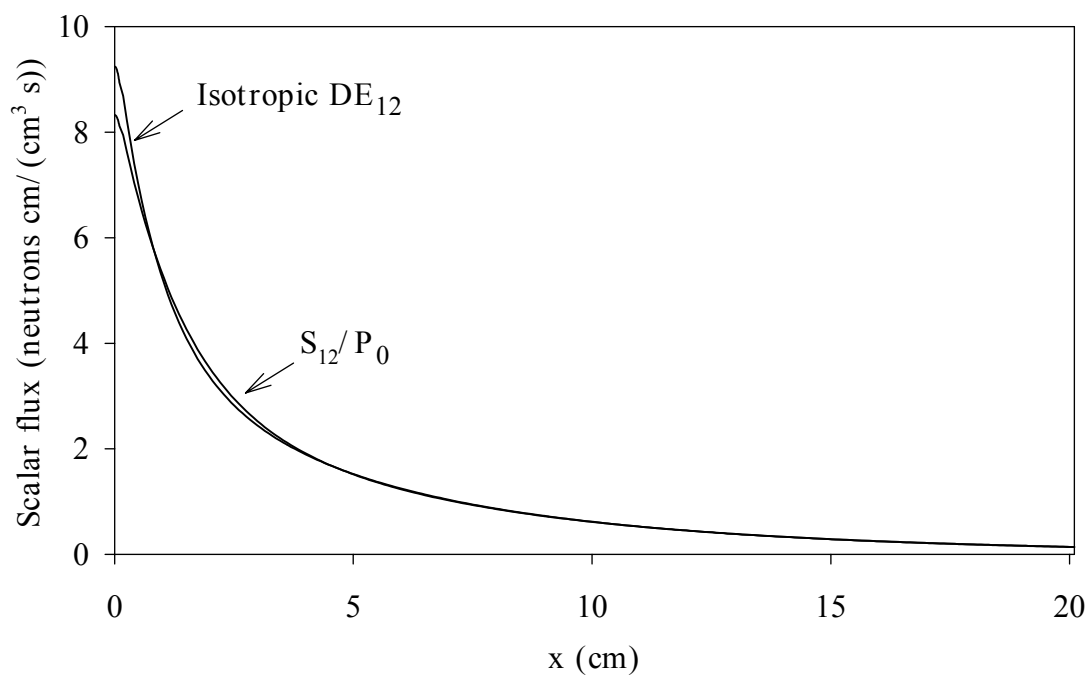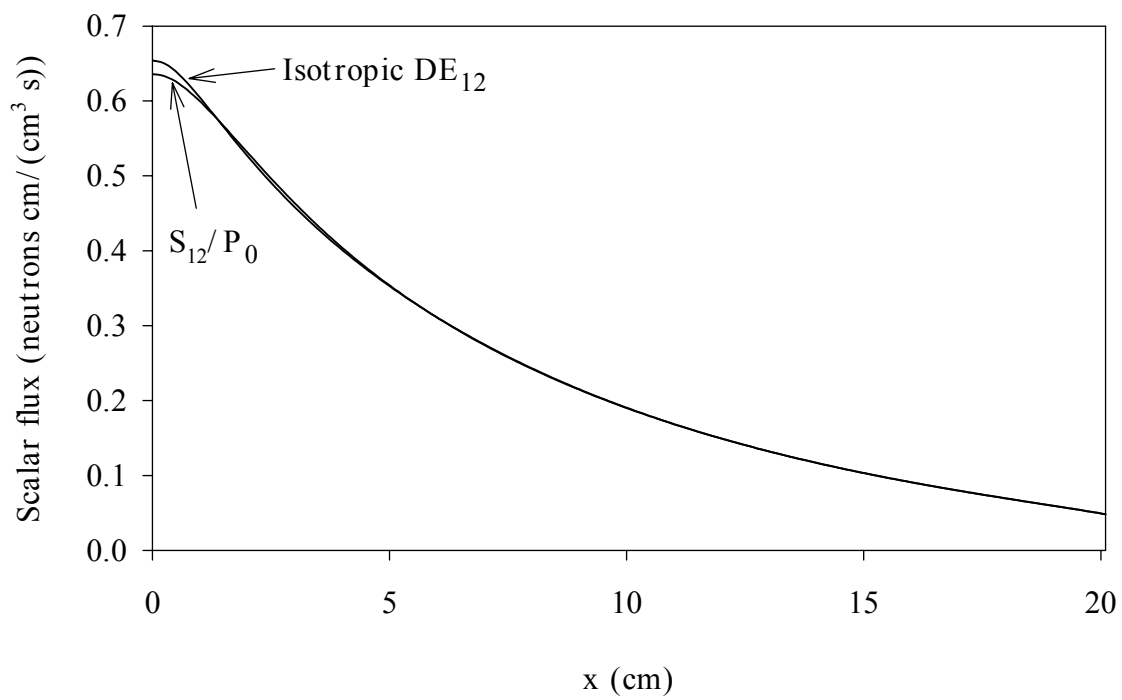
Figure 12: Isotropic comparison for group 1

Figure 13: Isotropic comparison for group 2
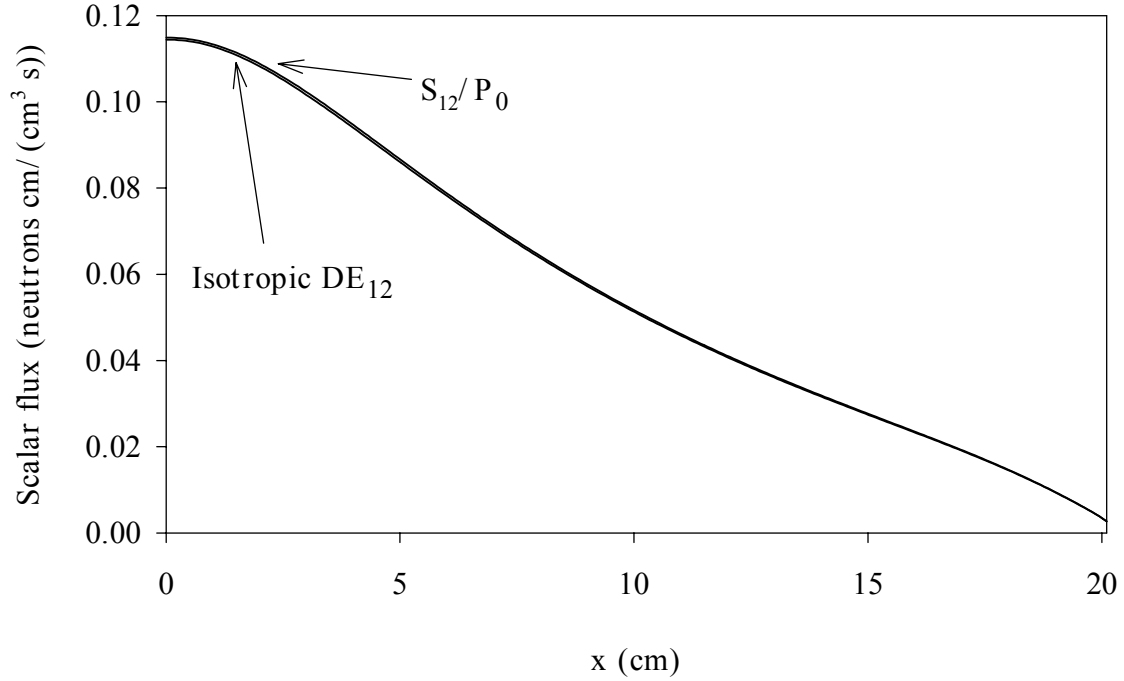
Figure 14: Isotropic comparison for group 28

The good agreement between both the discrete elements and the discrete ordinates for all three energy groups demonstrates DE_{12} is an adequate resolution compared to the discrete ordinates S_{12}.

VI.1.2: Anisotropic Comparison

The anisotropic comparison includes a Monte Carlo multi-group transport calculation using PAX_{64} cross sections. Energy groups 1 and 2 exhibit a computational artifact for both discrete ordinates and discrete elements compared to the Monte Carlo solution for the scalar flux due to the optically thin source region (in these groups). In one-dimensional transport with a thin source, much of the contribution to the scalar flux in and near the source region arises from neutrons traveling nearly perpendicular to the axis ($|m| = 1$). The Monte Carlo simulation includes particles emitted with $|m|$ near or equal to zero, but the discrete ordinates (S_n quadratures) and discrete elements methods need very high angular resolution (many elements or ordinates) to include ordinates close enough to perpendicular near-perpendicular contribution to the scalar flux.

Instead of using the typical discrete ordinates, S_n, quadrature based on a Gauss-Legendre quadrature rule (in one-dimension), a two angular region Gauss-Legendre rule could be used. The discontinuity in the angular flux at $m = 0$ can be better approximated using a double S_n quadrature rule (DS_n), such as the DS_6 quadrature rule given in appendix E. The DS_6 quadrature with the P_5 Legendre expansion for the group scatter cross section has been included to examine the effects of a quadrature rule that better approximates the discontinuity at $m = 0$.
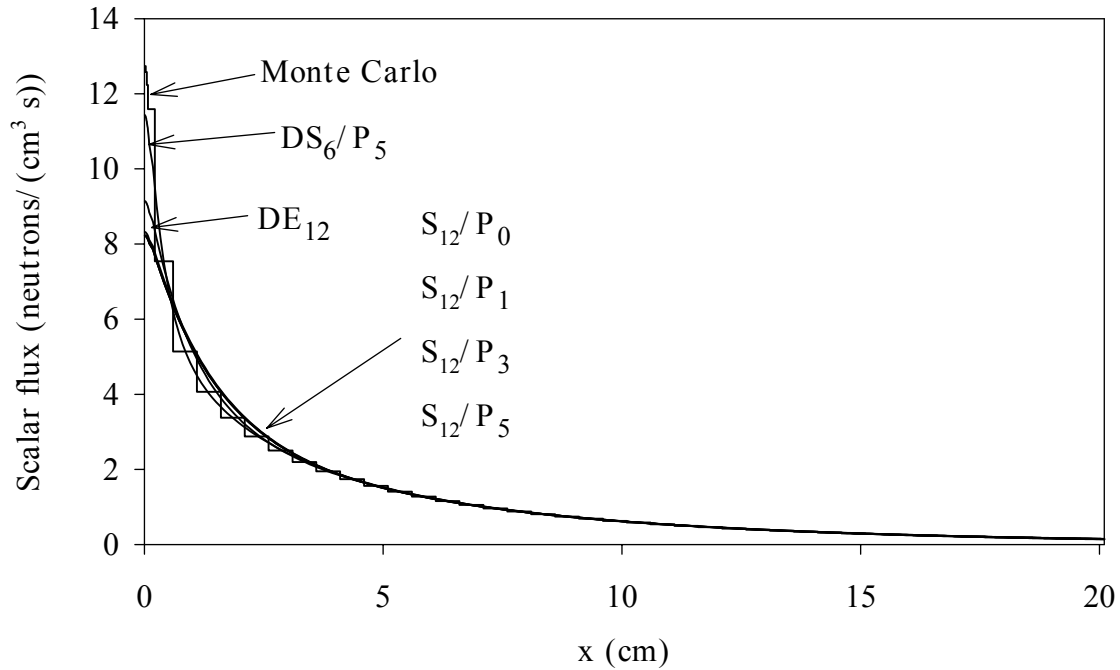
Figure 15: Energy group 1 anisotropic comparison

The first energy group exhibits the angular quadrature artifact in the scalar flux, although the DS_6 is significantly better than the DE_{12} or the any of the S_{12} quadratures. Near the source region, the discrete elements and the discrete ordinates underestimate the scalar flux. Note that the DE_{12} is a better approximation than the S_{12} quadratures.

Although the DS_6 quadrature is qualitatively a better approximation to the scalar flux in energy group 1 than DE_{12}, an angular flux comparison demonstrates the negativity associated with the P_5 Legendre expansion for the group scatter cross section. Figure 16 through Figure 18 show the angular flux as a function of both space

and the ordinate or element. Note that the angular flux is an angle integrated value for the discrete elements and a point value for the discrete ordinates.
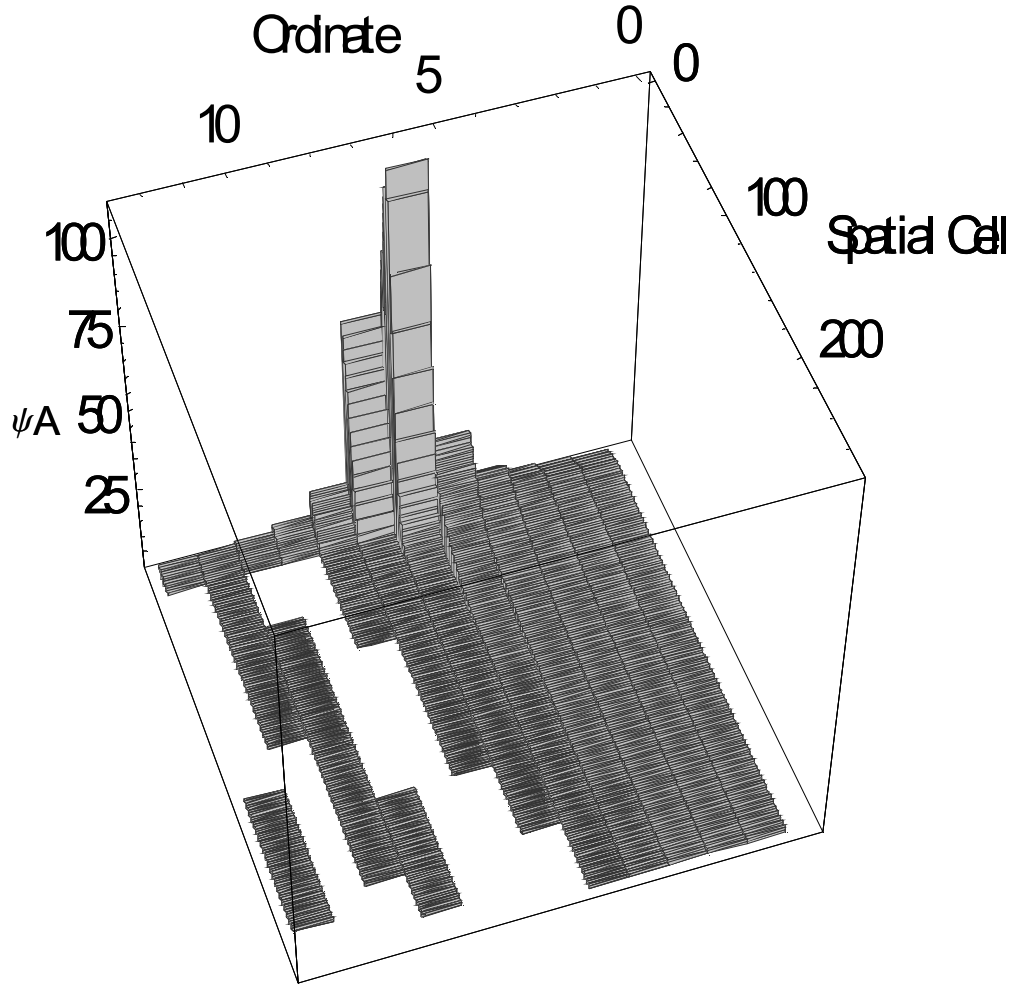
Figure 16: Energy group 1, DS_6/P_5 positive angular flux

The white areas in the plot are negative values in the angular flux arising from the P_5 Legendre expansion for the group scatter cross sections. The negative values for the angular flux do not contribute significantly to the scalar flux, but are completely unphysical. The negative angular flux is plotted in Figure 17.
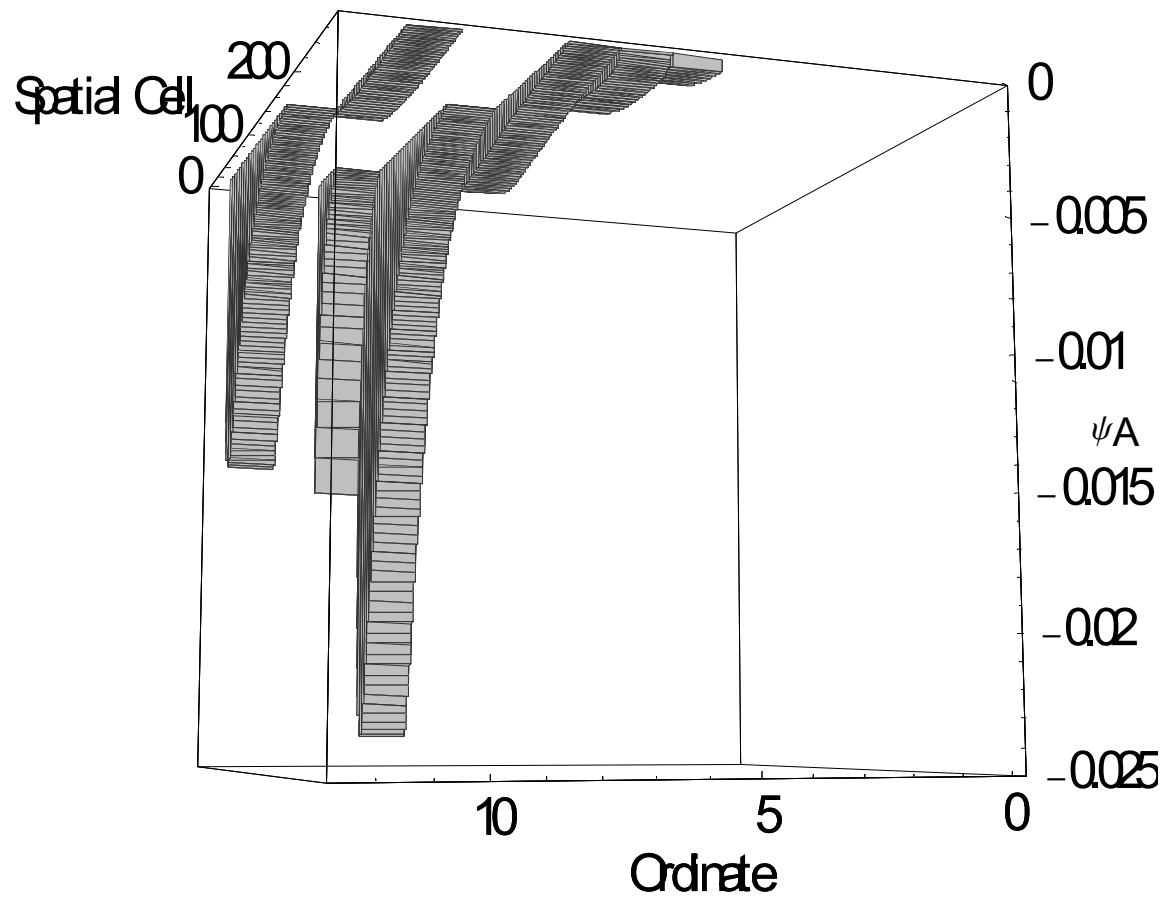
Figure 17: Energy group 1, DS_6/P_5 negative angular flux

The DE_{12} angular quadrature with the PAX_{64} cross sections result in positive angular fluxes throughout the entire problem when a source is present. The negative, unphysical angular flux is present in the DS_6/P_5 and not in the DE_{12}.
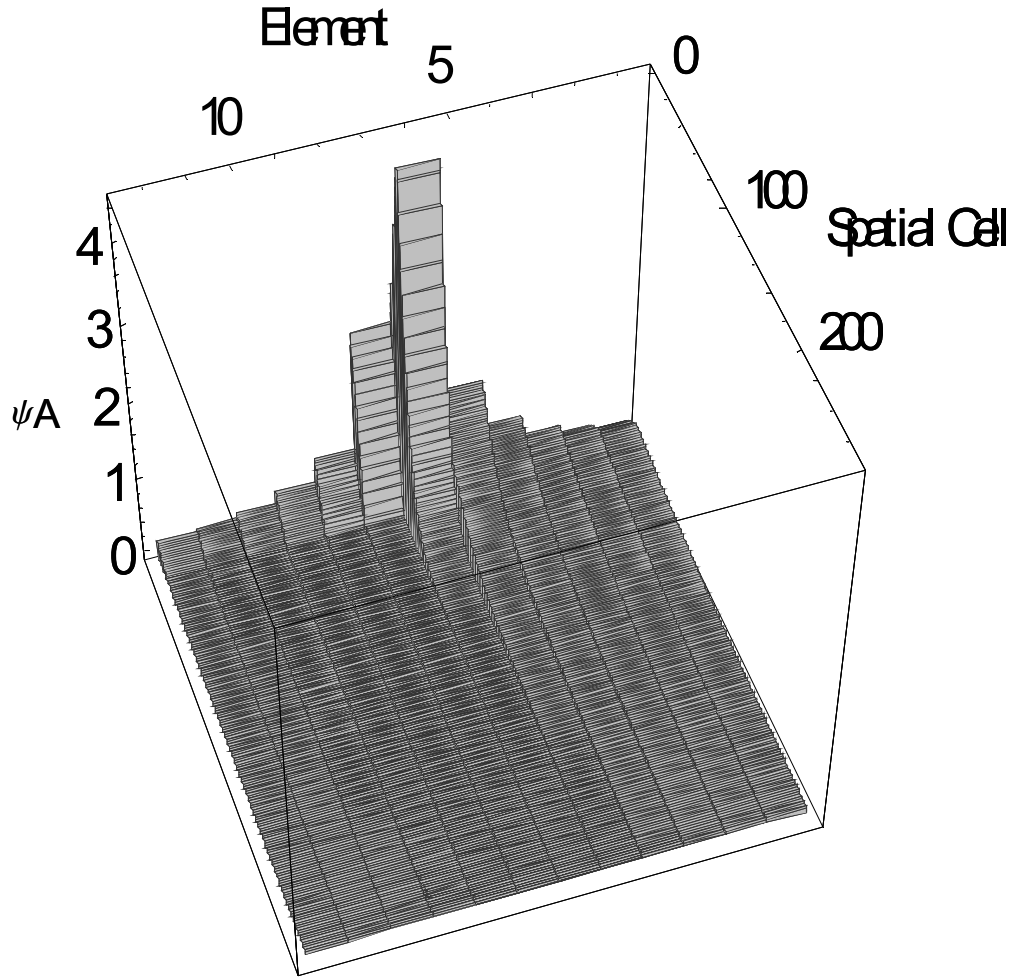
Figure 18: Energy group 1, DE$_{12}$ angular flux

Energy group 2 is used for two comparisons, the importance of the anisotropy to the scalar flux solution (thus motivating my work in investigating anisotropic scatter cross sections) and the point-wise convergence of the scalar flux when using the truncated Legendre expansions. The down-scatter source from group 1 is highly anisotropic and the scalar flux solution is incorrect for the isotropic approximation (shown as S$_{12}$/P$_0$).
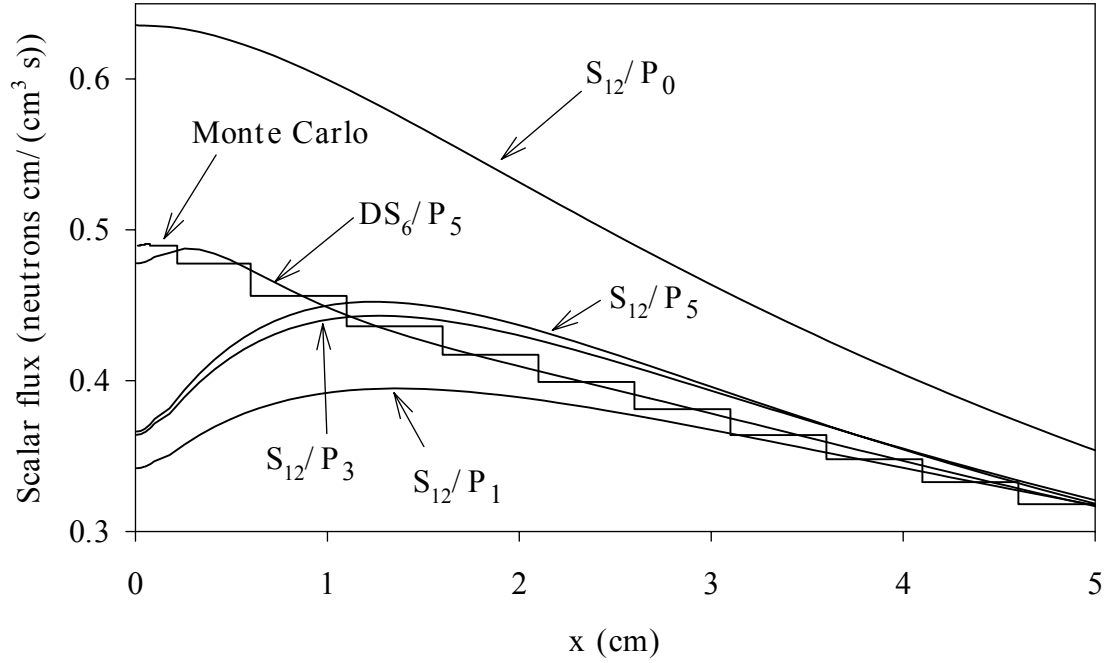
Figure 19: Energy group 2 with discrete ordinates

The point-wise convergence of the scalar flux when using discrete ordinates with truncated Legendre expansions is evident for the typical S_n quadrature. The DS_6 discrete ordinate quadrature is a good approximation for the scalar flux. But, the S_{12} quadratures are not converging uniformly to the scalar flux solution when the truncation order of the Legendre expansion is increasing. The P_3 approximation is closer to the Monte Carlo scalar flux solution for spatial positions greater than 1 cm and the P_5 approximation is closer for spatial positions less than 1 cm. The P_0 and P_1 approximations do not show any uniform convergence to the scalar flux compared to the other truncated Legendre expansions. Thus, different discrete ordinates quadratures (S_{12} and DS_6) combined with different truncated Legendre expansions do not converge uniformly to the scalar flux solutions—leading to the art form of choosing an appropriate truncation order and discrete ordinate quadrature set.

Having shown the non-uniform convergence to the Monte Carlo solution for the scalar flux, an investigation of the convergence was made for the discrete elements approximations using the PAX_{64} cross sections. The scalar flux for five discrete elements quadratures was compared to the scalar flux estimate from Monte Carlo in

energy group 2. The discrete elements angular quadratures are converging towards the Monte Carlo estimate for the scalar flux.
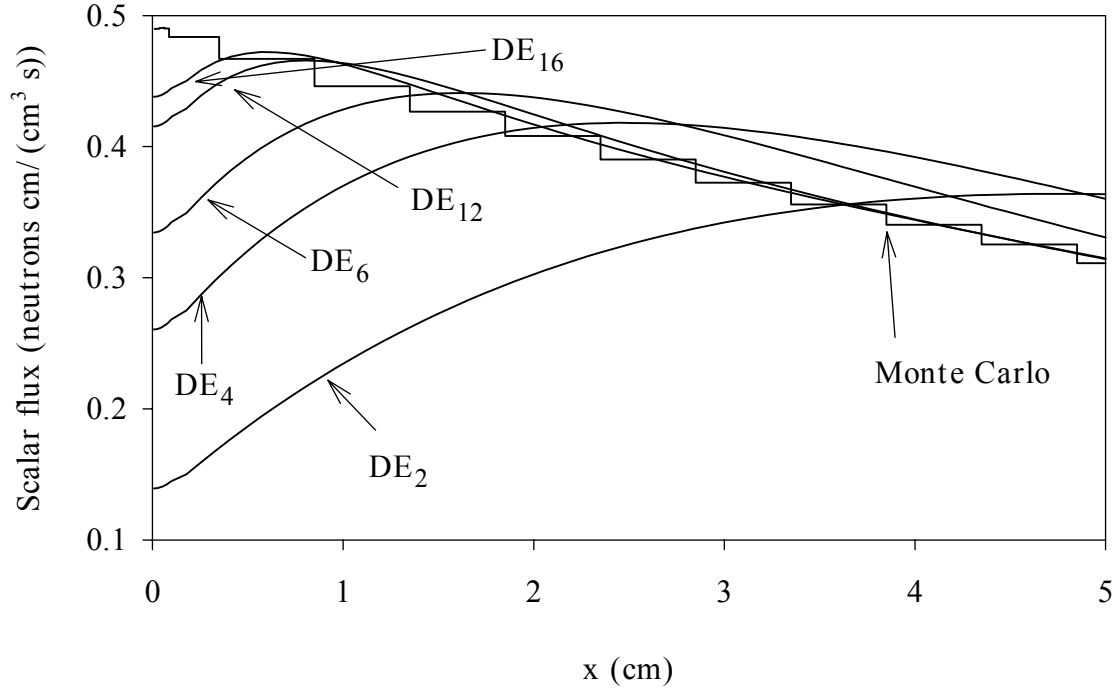
Figure 20: Energy group 2 with discrete elements

Energy group 28 shows the continued importance of the anisotropic cross sections. Although the P_1 expansion is different from the other calculations, the discrete elements and discrete ordinates calculations match the Monte Carlo estimate of the scalar flux closely.
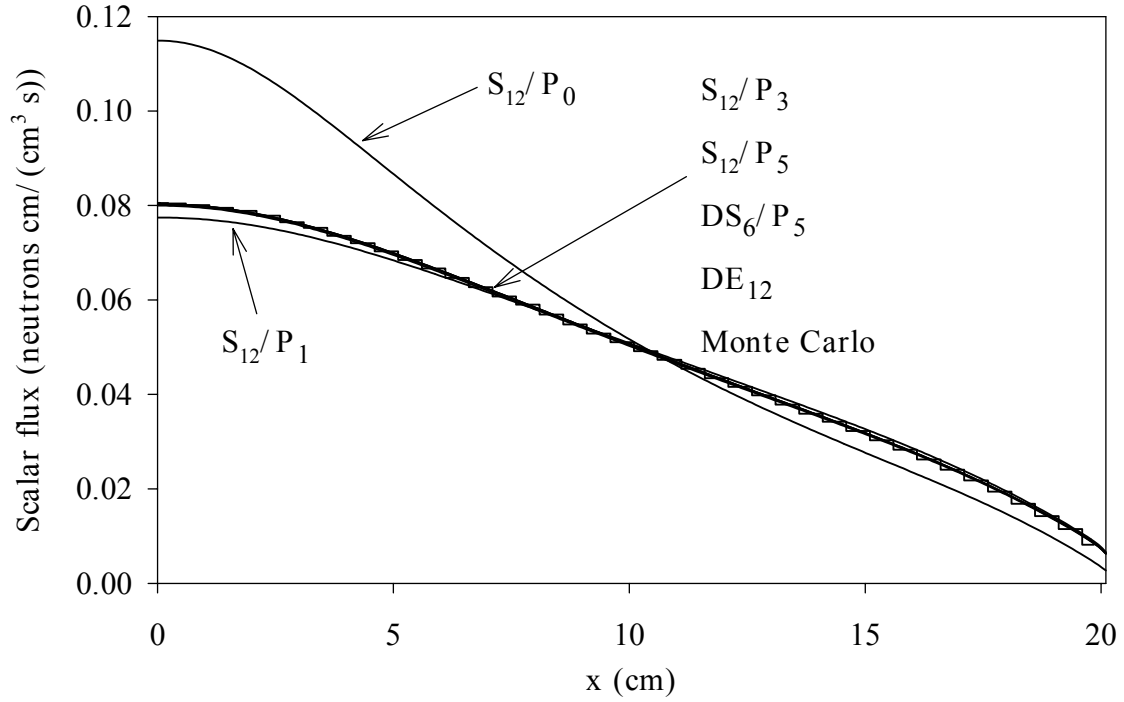
Figure 21: Energy group 28 anisotropic comparison

The thin source in a water-medium test problem displayed two important features of the different discrete approximations to the scalar flux solution. The anisotropic scatter cross section dominates the shape of the scalar flux. And, the discrete elements approximation to the scalar flux is converging to the Monte Carlo solution while the discrete ordinates to the scalar flux using truncated Legendre expansions is not converging uniformly.

VI.2: TEST PROBLEM 2: MULTI-LAYER SHIELD

Five different effects were examined with the second test problem: negative scalar fluxes when using diamond difference spatial quadratures, incorrect scalar fluxes when using discrete ordinates with truncated Legendre expansions for the scatter cross sections, convergence to the wrong energy dependence when using truncated Legendre expansions, uniform convergence of the energy dependence with increased number of discrete elements, and the importance of low probability scatters to the energy dependence.

This problem used four materials as a shield for a high energy source. Figure 22 shows the diagram for test problem 2 where the dimensions are all in centimeters. The isotropic source in energy group 1 was distributed uniformly throughout the ^{56}Fe region. All of the examples used 96 equal-thickness spatial cells.
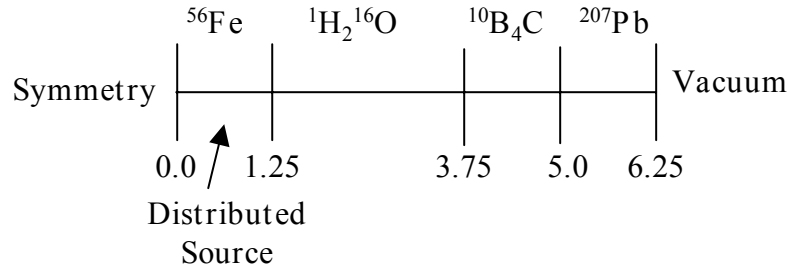
Figure 22: Multi-layer shield

VI.2.1: Diamond Difference Generates Negative Scalar Fluxes

The first effect examined was the negative scalar fluxes when the diamond difference (DD) spatial quadrature method was used. The scalar flux for an exponential characteristic (EC) spatial quadrature method is compared to the DD calculation for energy group 30 with both spatial quadrature methods using a discrete element angular quadrature with PAX$_{64}$ cross sections (ie. non-negative cross sections).
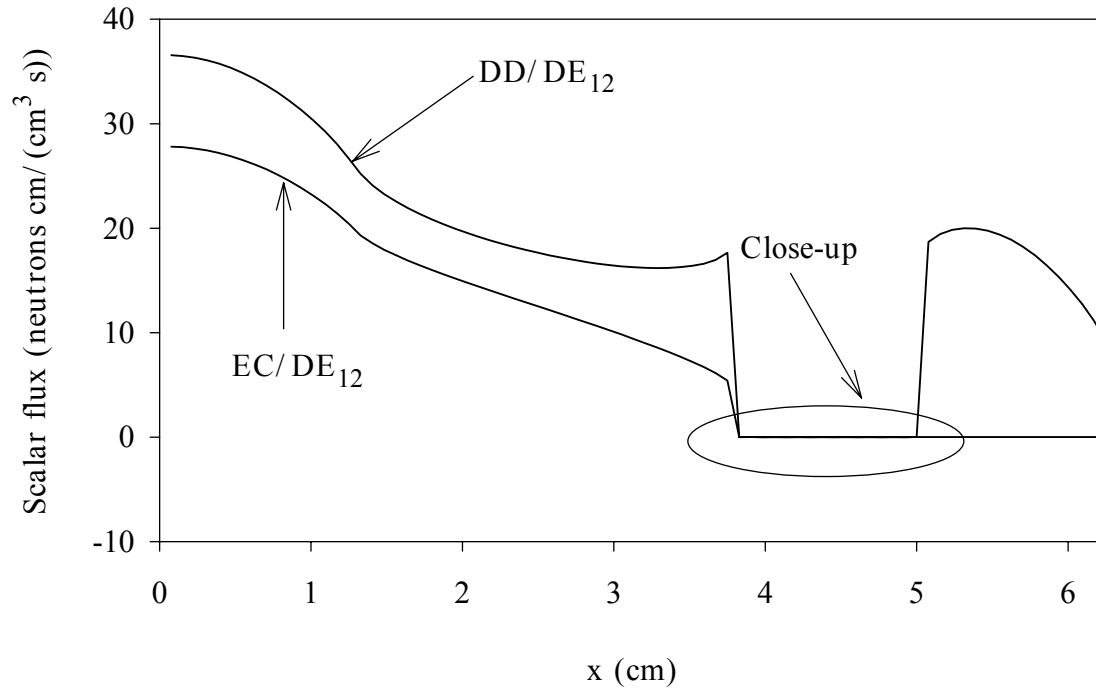
Figure 23: EC comparison to DD

The DD calculation is incorrect throughout the entire problem for this energy group. The scalar flux in the B_4C region (between 3.75 and 5.0 cm) is unphysical and oscillates between positive and negative values, as is seen in Figure 24 (an enlargement of the B_4C region).

The oscillations of the DD method in the B_4C region have led to a drastic overestimation of 8 orders of magnitude in the scalar flux in the ^{207}Pb region (between 5.0 to 6.25 cm). The DD method has failed to produce positive scalar fluxes even with non-negative group-to-group cross sections.
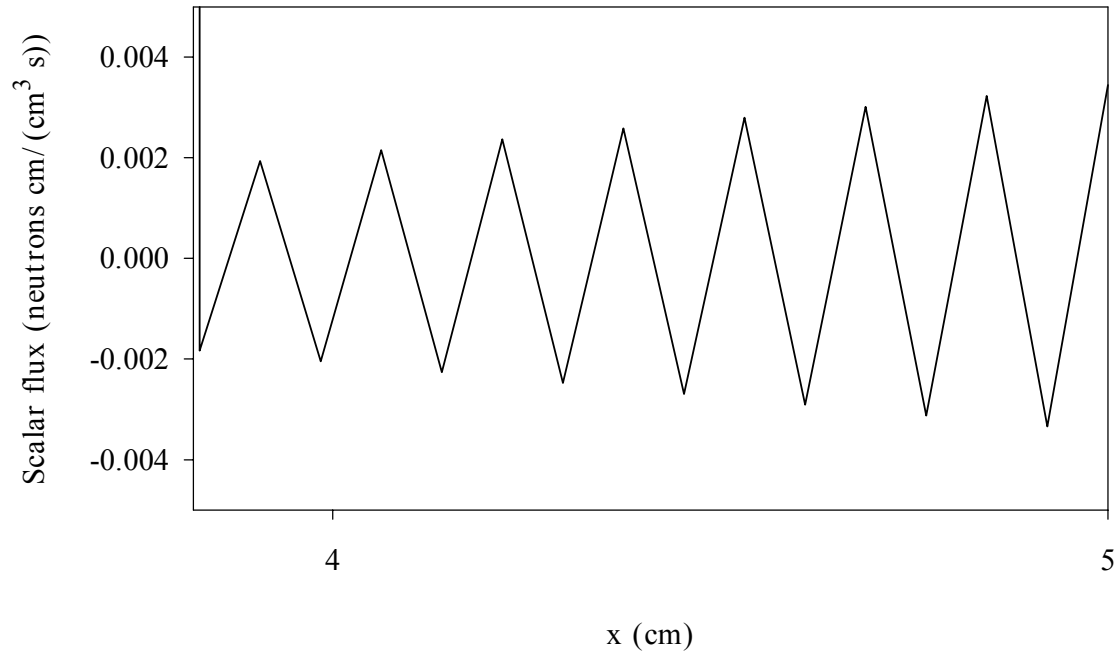
Figure 24: DD close-up of B$_4$C

The test problem was run with continued spatial refinements using DD to discover when the scalar flux in energy group 30 would no longer be negative. The DD scalar flux solution continued to have negative values for the scalar flux when over 5000 spatial cells were used—a physical thickness of just over 10 mm per cell. Higher refinements were not possible with the spatial transport code because the code was not written for efficient memory usage, but rather, it stores all variables to facilitate examination of them.

VI.2.2: Discrete Ordinates Compared to Discrete Elements

The step spatial quadrature method was used to compare discrete ordinates with truncated Legendre expansions for the cross sections to discrete elements using PAX$_{64}$ cross sections. The step method was used because it is a non-negative method (as opposed to DD) with non-negative cross sections. An EC calculation was also performed for comparison. The EC method is also non-negative, but the EC method cannot use negative cross sections and the step method can.

The multi-layer shield problem was run using the step spatial quadrature for both S_{12}/P_5 and DE_{12}. Energy group 30 was again examined and the results are shown in Figure 25.
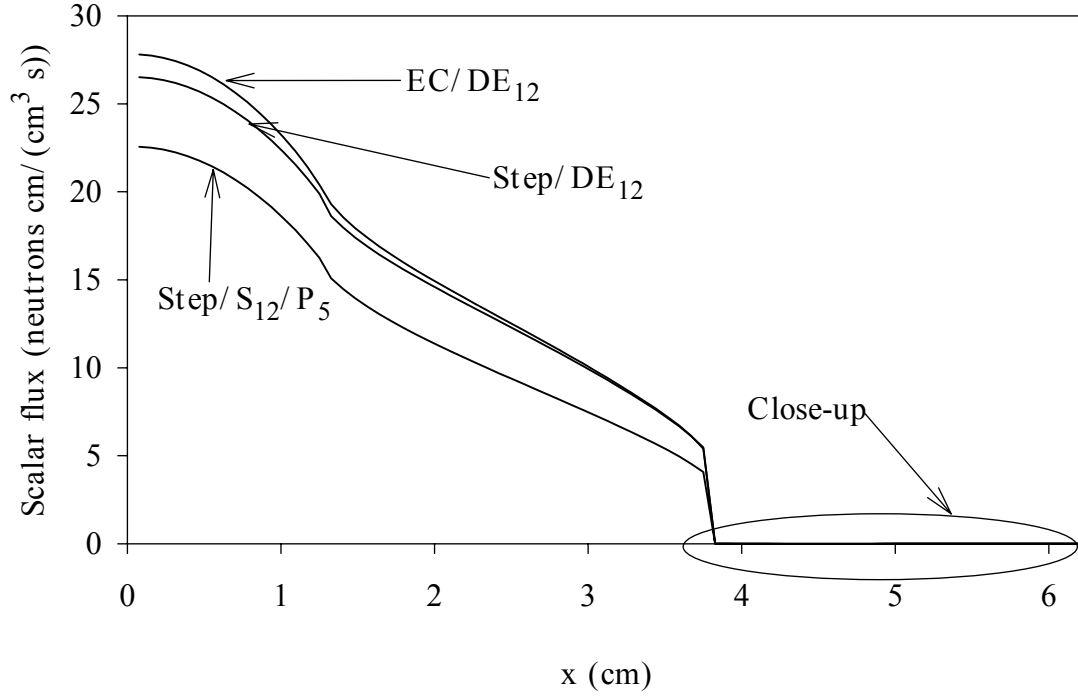
Figure 25: Step comparison to EC

The scalar flux for the step method is close to the EC scalar flux solution when both methods used the discrete elements angular quadrature. This indicates the inadequacy of the spatial mesh for the $\mathcal{O}(s\,\mathrm{D}x)$ step method as compared with the

$\mathcal{O}(s\,\mathrm{D}x)^4$ EC method. By comparison, the much larger difference between the step/DE_{12} and the step/S_{12}/P_5 results is significant. I attribute this difference to the inaccuracies of the discrete ordinates angular quadrature with a P_5 truncated Legendre expansion.
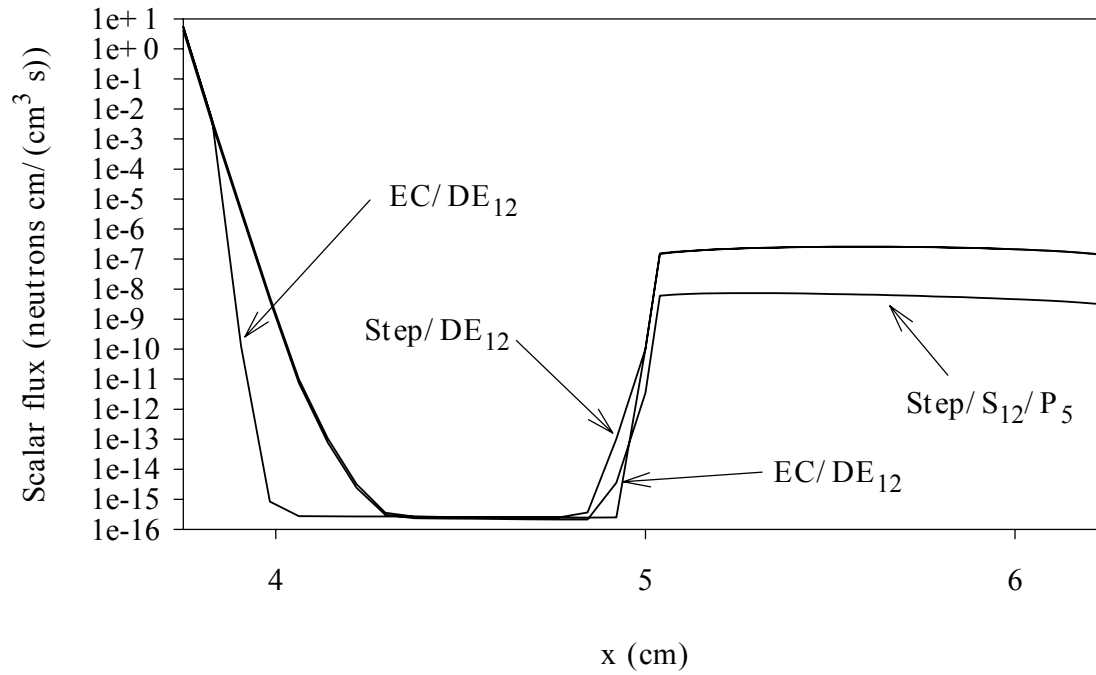
Figure 26: Close-up of step comparison to EC

An enlargement of the scalar flux solution for the B_4C and ^{207}Pb regions of the scalar flux shows the inaccurate scalar flux using the S_{12} angular quadrature with P_5 truncated Legendre expansion in the outer regions.

VI.2.3: Effects of Angular Quadrature Refinement on Energy Dependence

The effects of the angular quadrature refinement on the energy dependence were examined by comparing the energy dependence using a step/DE_{12} to four step/S_n/P_1 calculations. The EC/DE_{12} agreed with the step/DE_{12} calculation. The step spatial quadrature method is again used because of its non-negativity when using non-negative cross sections. The 30-group structure from appendix D is used in Figure 27 to plot the neutron current exiting the test problem at the vacuum boundary.
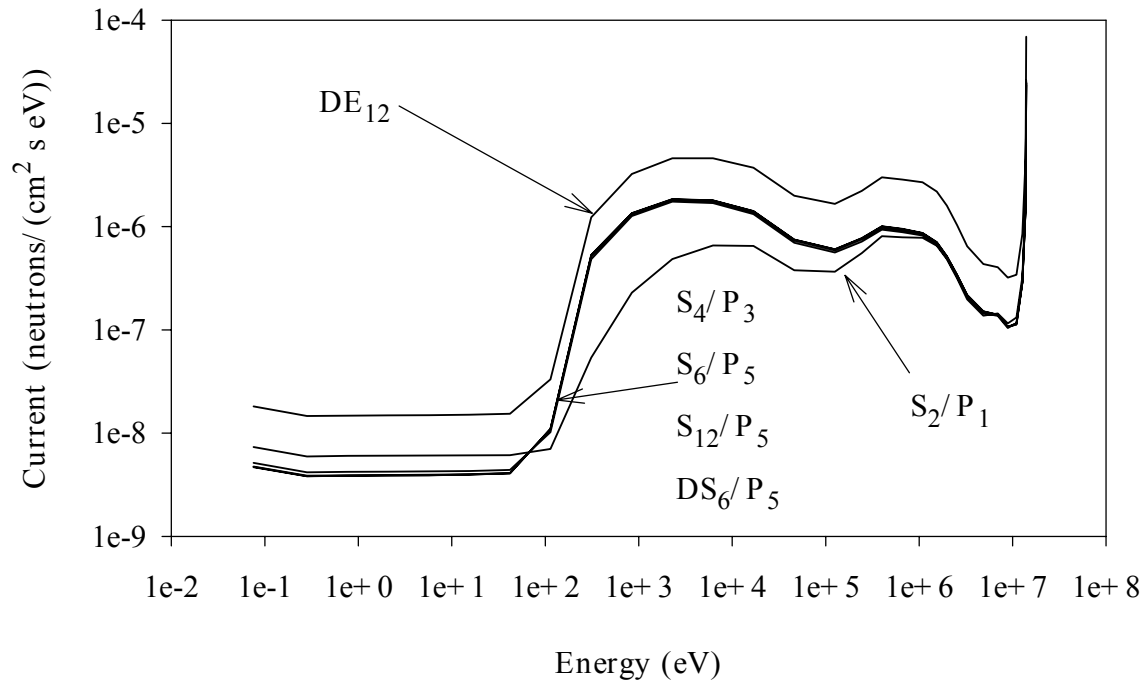
Figure 27: Effect of discrete ordinates angular resolution in energy dependence

The angular quadrature is not converging to the step/DE_{12} solution for the four step/S_n/P_l calculations. This is shown by the more accurate S_2/P_1 solution for energies less than 10 eV and the less accurate S_2/P_1 solution for energies greater than 10 eV. To investigate if the discrete ordinates solutions with the truncated Legendre expansions were consistently differing from the discrete elements solutions, a plot of the relative error e_{rel} of the discrete ordinates compared to the discrete elements was made in Figure 28, where

$$e_{rel} = \frac{2\left(J_{DE_{12}} - J_{S_n/P_l}\right)}{\left|J_{DE_{12}}\right| + \left|J_{S_n/P_l}\right|}.$$ (47)
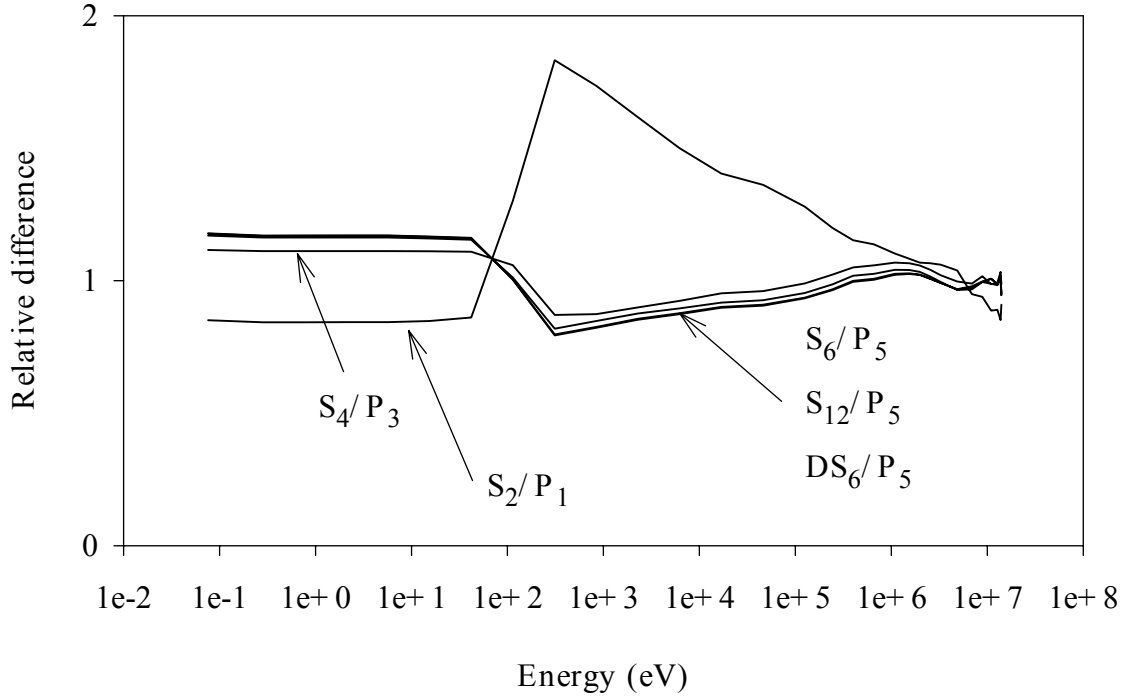
Figure 28: Relative difference between step/S_n/P_1 and step/DE_{12}

The relative difference between the step with different S_n/P_1 combinations and the step spatial quadrature with DE_{12} shows that some combinations are less accurate at some energies and more accurate at other energies. The inclusion of the double S_n quadrature (DS_{12}) shows that the artifact discussed in test problem 1 is not dominating the error in the solution. Instead the difference between the step/DE_{12} and the step/S_n/P_1 can be attributed to the truncated Legendre expansions for the group scatter cross sections.

VI.2.4: Angular Refinement of Discrete Elements with Energy Dependence

Convergence of the discrete elements angular quadrature is expected as more elements are added. For this test problem, Figure 29 shows the EC spatial quadrature methods with DE_2, DE_4, DE_6, and DE_{12}.
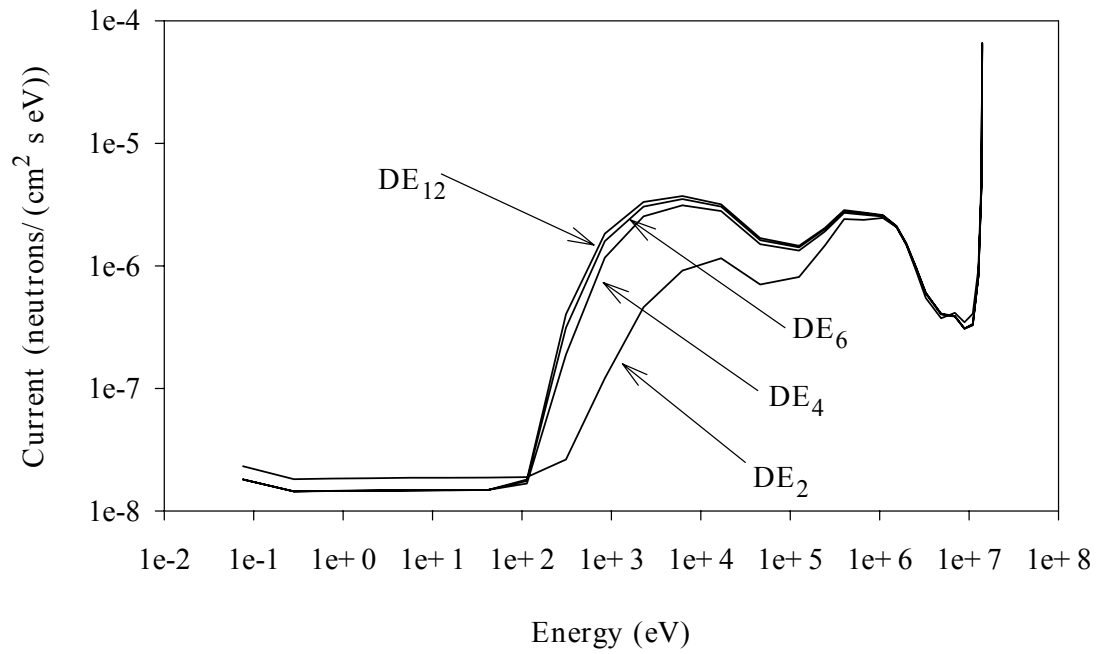
Figure 29: Effect of discrete elements angular resolution in energy dependence

In a similar comparison to Figure 28, relative differences between the DE_2, DE_4, and DE_6 to the DE_{12} solution are shown in Figure 30.
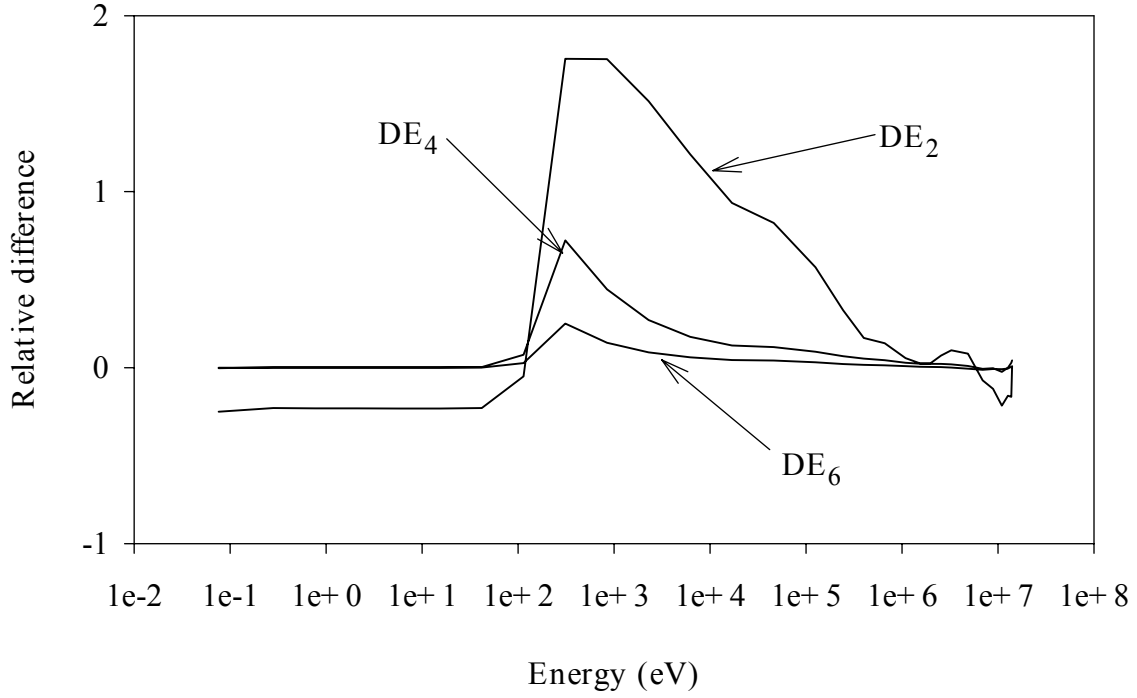
Figure 30: Relative difference between DE_{12} and DE_2, DE_4, and DE_6

The error in the DE_2 calculation is dominated by its nearly isotropic approximation. The angular quadrature for DE_2 is insufficiently angularly resolved for this test problem. The DE_4 and the DE_6 are converging to the DE_{12} solution for the energy dependence of the current at the vacuum boundary.

VI.2.5: Energy Group Refinement

The effects of refining the energy groups for this test problem were investigated. Three different comparisons with energy group refinement were made: EC with DE_{12}, step with S_{12}/P_5, and step with DE_{12}. The energy meshes, with 30, 59, and 117 groups, were made using the energy group structures defined in appendix D.
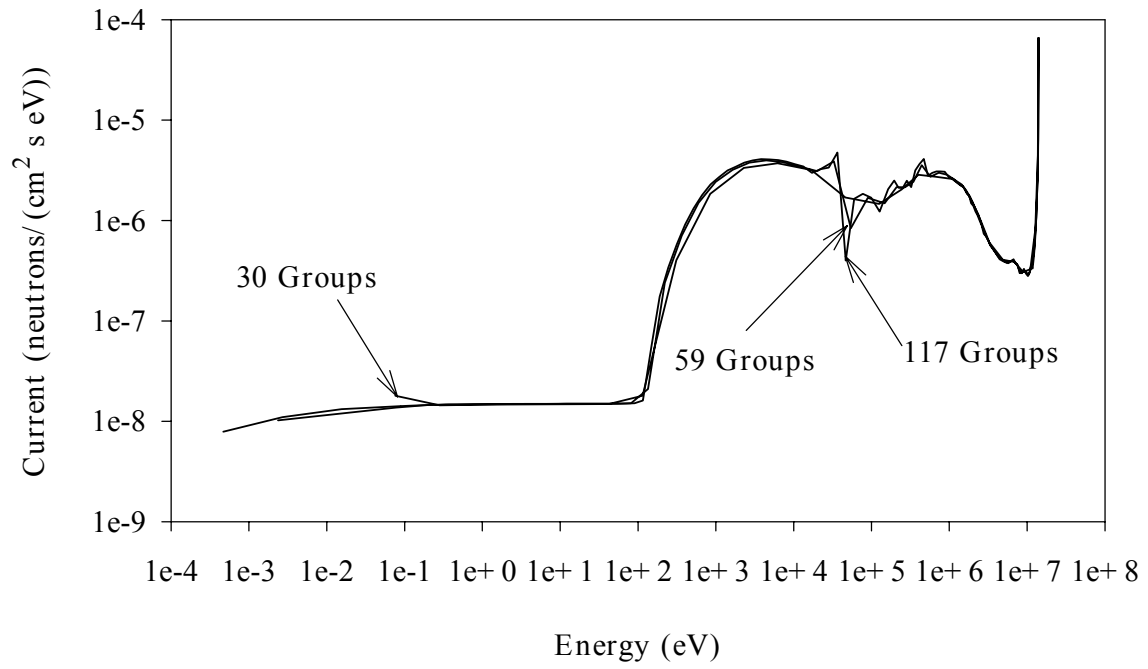
Figure 31: Energy dependence for EC with DE_{12}
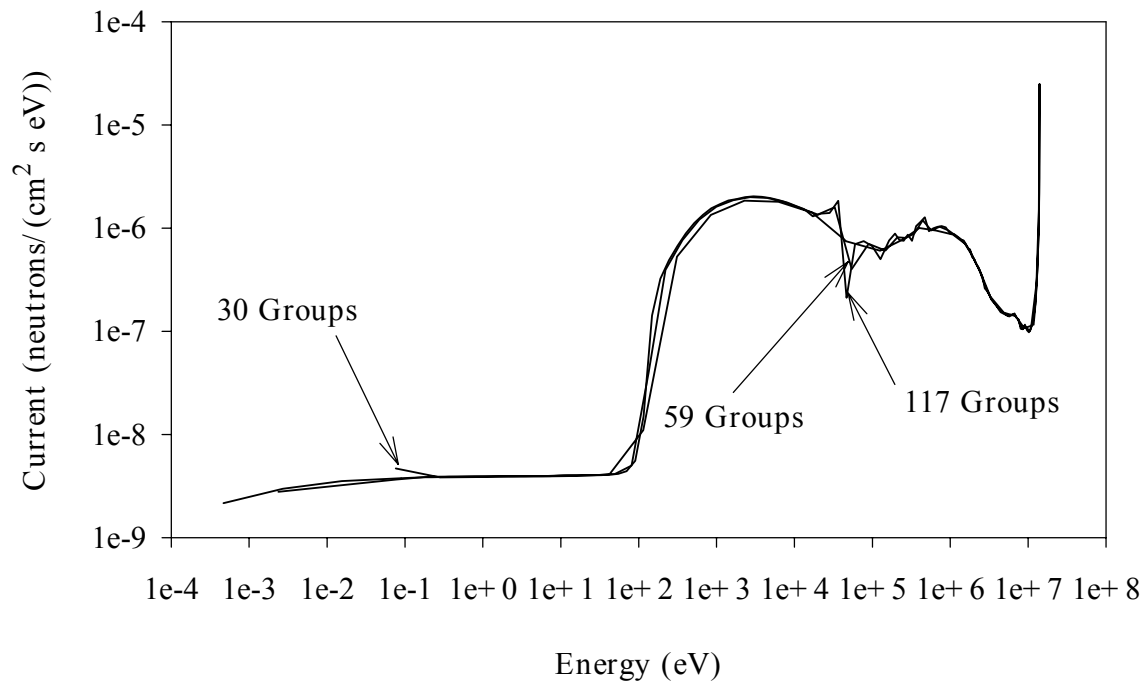
Figure 32: Energy dependence for step with S_{12}/P_5
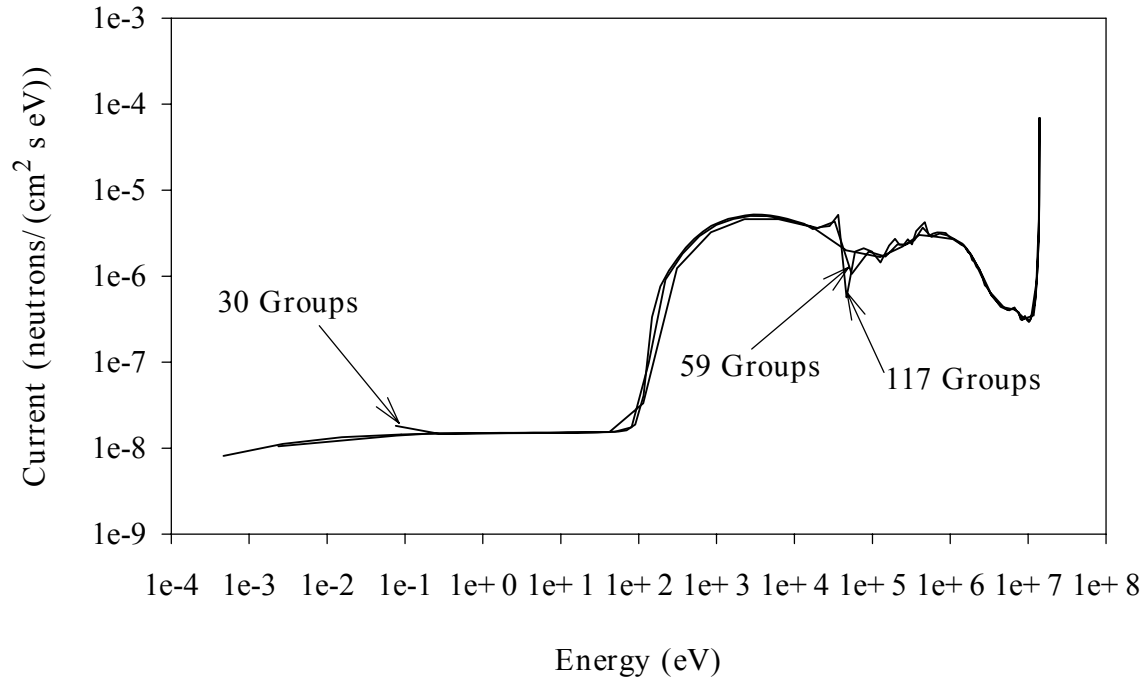
Figure 33: Energy dependence for step with DE_{12}

All three energy dependencies are changing with the refinement in energy group. Although the step/S_{12}/P_5 appears qualitatively similar, the comparison of step/S_{12}/P_5 to the step/DE_{12} in section VI.2.3 demonstrated that the current was incorrect. The energy dependence is changing for both the step/DE_{12} and EC/DE_{12} calculations, as the energy group structure is refined. Therefore, the energy group structure may not be sufficiently refined in energy to accurately determine the energy dependence of the current at the vacuum boundary, depending on the application.

VI.2.6: Attributing Features in the Energy Dependence

A comparison was made between the rightward partial current entering the ^{207}Pb region and the rightward partial current at the vacuum boundary because the refinement in energy in Figure 31 showed an increasingly variable solution in the energy dependence in the energy range of 10 keV to 1 MeV. The comparison was made using the 117-group structure presented in appendix D. Figure 34 shows the rightward current at both the vacuum boundary and the B$_4$C/^{207}Pb boundary.
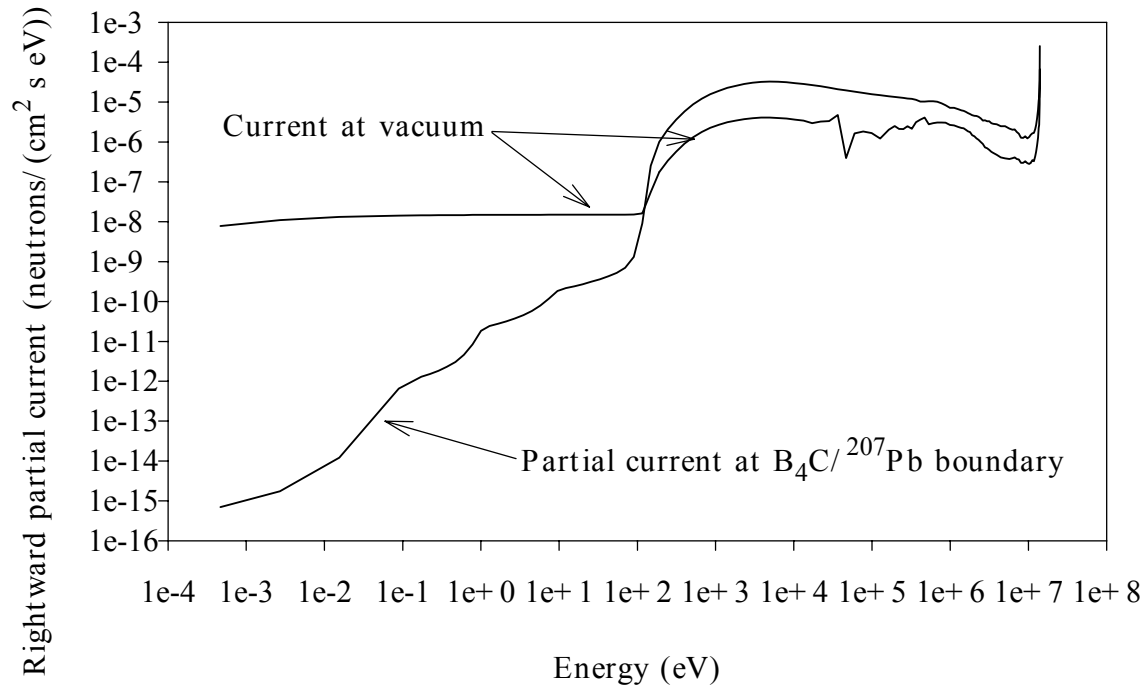
Figure 34: Comparison of energy dependence of rightward partial current at two spatial locations

Without any intrinsic source in the ^{207}Pb region, the variation of the energy dependence of the current exiting at the vacuum boundary arises from either the cross section of ^{207}Pb or the current flow from the B$_4$C. Figure 34 shows that the current entering the ^{207}Pb from the B$_4$C is smooth in the 10 keV to 1 MeV energy range in comparison to the current at the vacuum boundary. Due to the smoothness of the entering flux and the large variation of the total cross section of ^{207}Pb shown in Figure 35 in this energy range, I attribute the variation in the energy dependence of the rightward partial current at the vacuum boundary to the ^{207}Pb cross section.
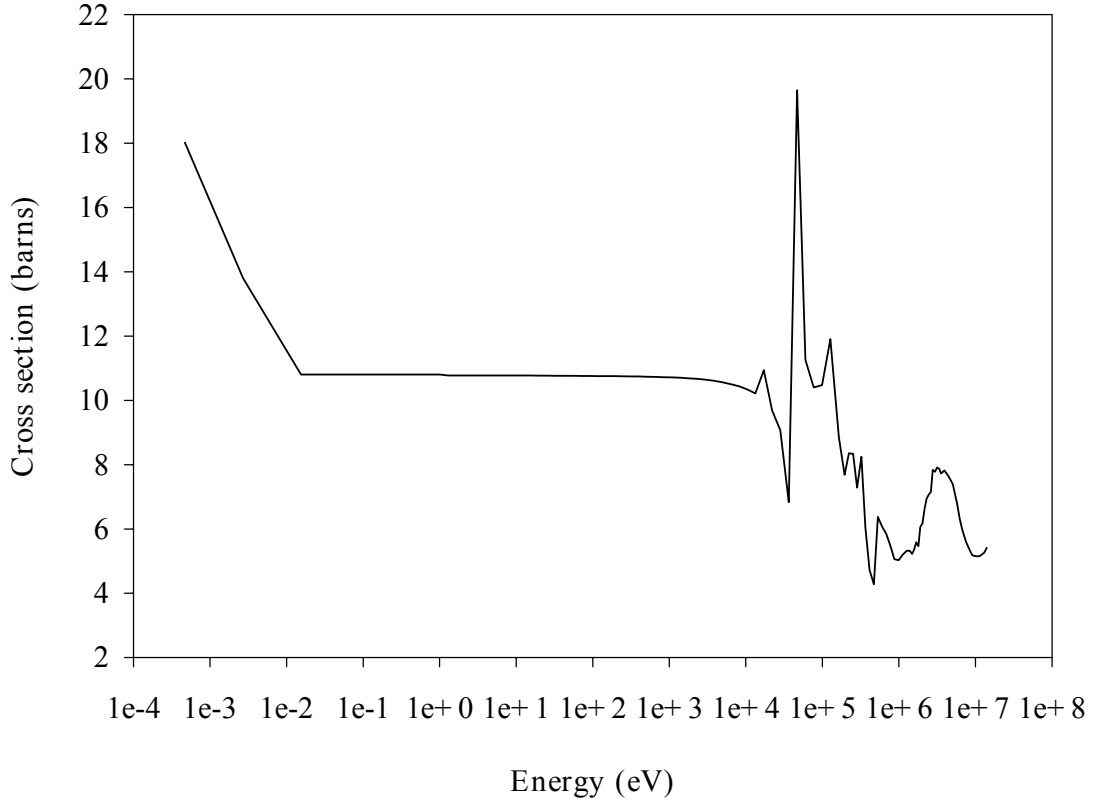
Figure 35: ^{207}Pb total cross section

Figure 34 shows that energy dependence for energies less than 100 eV of the rightward partial current at the vacuum boundary is fairly flat compared to the current exiting the B$_4$C region. Because the current, in this problem, exiting at the vacuum boundary can only arise from inflow from the B$_4$C region or down-scatter within the ^{207}Pb region, the low energy current must be down-scatter because the inflow current is negligible.

To examine the contributions to the down-scatter source, a calculation with the 30-group structure in appendix D.2 was used. The 30-group calculation has similar, but less resolved energy dependence of the currents. The ^{207}Pb region down-scatter contribution to group 30 from each incident group was calculated as an angle-integrated, region-integrated down-scatter source. To demonstrate the low probability of scatter from the incident group, the fractions of the scatter cross section from the incident group to group 30 are also presented in Table 2.

Table 2: Down-scatter source contribution to ^{207}Pb region

Incident Group	Down-Scatter Source	Fraction of Scatter from Incident Group to Group 30
1	6.755617E-08	1.274419E-09
2	2.545111E-08	1.320084E-09
3	1.559567E-08	1.406711E-09
4	1.341229E-08	2.325594E-09
5	9.901283E-09	2.036932E-09
7	9.066829E-14	9.475451E-15
8	6.584222E-13	1.225620E-13
9	1.137028E-13	1.919159E-14
29	4.874568E-10	9.697575E-03

The group-29 down-scatter source was smaller than the down-scatter source for each incident group 1 through 5. Therefore, I attribute the energy dependence of the current below 100 eV to the down-scatter source from energies in the range of 7.79 to 14.1 MeV. Low-probability scatters at the high energies are dominating the energy dependence at low energies of the current at the vacuum boundary. Among 10^9 group-one neutrons that scatter in ^{207}Pb, only 1.3 neutrons scatter directly into group 30. Nevertheless, in this problem, more than half (51%) of the neutrons that enter group 30 in the lead do so by direct scatter from group 1.

VII. Summary and Conclusions

Nonlinear, accurate, and robust spatial quadrature schemes for the multi-group discrete ordinates method, such as the exponential characteristic method, provide physically meaningful, non-negative fluxes given non-negative incident fluxes, emission sources, and scattering cross sections. Conventional techniques based on Legendre expansions of the scattering cross sections cannot be relied upon to provide such cross sections. Multi-group discrete element bin-to-bin scattering cross sections, introduced by DelGrande and Mathews (7), are non-negative if calculated from non-negative scattering cross sections $s_s(E' \to E, m)$. These cross sections eliminate, or at least strongly ameliorate, many other artifacts of conventional discrete ordinates cross sections and angular quadratures, as discussed by DelGrande and Mathews (7).

The original objective of this effort was to develop an accurate and efficient scheme for calculating the cross sections directly from the data in ENDF/B-VI (18). This would make it possible to use the exponential characteristic method, and similar methods, for anisotropic scattering in real materials. This has been accomplished.

DelGrande and Mathews used Monte Carlo simulations that sampled from ACE files (13). I explored enhancing his approach by introducing variance reduction schemes, but abandoned that approach. It is easy to obtain modest accuracy in the cross sections for the likely scatters, but to do so for one-in-a-million scatters seems unachievable. The multi-layer shield problem presented here shows that such unlikely scattering events can be the dominant source of particles in at least some energy groups in some problems, so I sought a method that would calculate such cross sections accurately and efficiently.

By separating the angular and energy dependences of the discrete elements and energy group structure, I found it possible to formulate the cross sections such that the maximum nesting of integrations was only three deep, and usually only two. Nested adaptive numerical quadratures have proven effective in making these calculations efficient while providing user-set convergence tolerances. This has been implemented in FORTRAN-95, demonstrating the computational practicality of the approach. An efficient code for generating the scattering-cosine-dependent conditional element-to-element scattering probabilities, $h_{n' \to n}(m)$, is the only piece needed for efficient

68

generation of bin-to-bin cross sections for multi-dimensional transport calculations. Many approaches to defining partitions of the unit sphere into discrete elements are possible; each would need its own code for the element-to-element conditional probabilities.

In order to validate my computational techniques and the code that implemented them, it was necessary to generate Legendre coefficients for group-to-group cross sections and compare them with the values produced by NJOY.

By introducing a scattering operator, it became clear that one code could provide not only bin-to-bin cross sections and Legendre moments, but also group-to-group cross sections approximated as piecewise-average functions of the scattering cosine, which I call PAX cross sections. The PAX cross sections are one of the major contributions of this work. They are readily computed and tabulated and can then be used to produce bin-to-bin cross sections and Legendre moments. Furthermore, the PAX cross sections could be used directly for sampling scattering in multi-group Monte Carlo transport simulations, or could be used to generate equal-likelihood scattering intervals for use in such codes.

The code written for this research is not a production code. Some of the ENDF/B-VI scatter laws are not yet implemented. Also, writing independent modules for computing Legendre moments, bin-to-bin cross sections, and piecewise-average cross sections could substantially reduce run times. Nevertheless, the practicality and some of the benefits of my methods have been demonstrated successfully using this code.

The impact of these new approaches to generating and using scattering cross sections, if adopted by the community, will be to provide physically meaningful and more accurate cross sections and physically meaningful and more accurate fluxes from radiation transport calculations that use them.

Appendix A: Variable Definitions

A.1: CONTINUOUS REPRESENTATIONS

$$\psi\left(\vec{r}, E, \hat{\Omega}\right) \tag{48}$$

The angular flux is a distribution function in space, energy, and angle. It can be described as a neutron path length rate density with units such as $\dfrac{neutron\,cm}{s\,cm^3\,eV\,steradian}$.

$$\sigma^s\left(\vec{r}, E \rightarrow E, \hat{\Omega}\cdot\hat{\Omega}\right) \tag{49}$$

The continuous scatter cross section is a point function in space, incident energy, and incident direction. It is distribution function with respect to the secondary energy and the secondary direction. The continuous scatter cross section has units of $\dfrac{barns}{eV\,steradian}$.

A.2: ENERGY GROUP REPRESENTATIONS

$$\psi\left(\vec{r}, E, \hat{\Omega}\right) \approx \psi_g\left(\vec{r}, \hat{\Omega}\right)F(E), \qquad E_g \le E \le E_{g-1} \tag{50}$$

where the energy-dependent spectral weighting function is normalized by

$$\int_{\Delta E_g} dE\, F(E) = 1 \tag{51}$$

and

$$\int_{\Delta E_g} dE = \int_{E_{g-1}}^{E_g} dE \tag{52}$$

The group angular flux, ψ_g, is a distribution function in space and angle, and a bin integrated function in energy. It has units of $\dfrac{neutron\,cm}{s\,cm^3}$.

70

$$\sigma^s_{g'g}\left(\vec{r},\hat{\Omega}'\cdot\hat{\Omega}\right)=\frac{\int_{\Delta E_{g'}} dE'\int_{\Delta E_g} dE\,\sigma^s\left(\vec{r},E'\rightarrow E,\hat{\Omega}'\cdot\hat{\Omega}\right)\Phi(E')}{\int_{\Delta E_{g'}} dE'\,\Phi(E')}\tag{53}$$

The group scatter cross section is a point function in space and incident direction, and a spectrum-weighted average over energy. It is a distribution function with respect to the secondary direction and a bin integrated function with respect to the secondary energy. The group scatter cross section has units of $\dfrac{barns}{steradian}$.

A.3: DISCRETE ELEMENT REPRESENTATIONS

$$\psi_g\left(\vec{r},\hat{\Omega}\right)\approx\frac{\psi_{n,g}\left(\vec{r}\right)}{\Delta\Omega_n}\tag{54}$$

where $\Delta\Omega_n$ is an element of solid angle. The discrete element, group angular flux $\psi_{n,g}$ is a distribution function in space and a bin-integrated function in energy and angle. It has dimensions of $\dfrac{neutron\,cm}{s\,cm^3}$.

$$\sigma^s_{n'n,g'g}\left(\vec{r}\right)=\frac{\int_{\Delta\Omega_n} d\Omega\int_{\Delta\Omega_{n'}} d\Omega'\int_{\Delta E_{g'}} dE'\int_{\Delta E_g} dE\,\sigma^s\left(\vec{r},E'\rightarrow E,\hat{\Omega}'\cdot\hat{\Omega}\right)\Phi(E')}{\Delta\Omega_{n'}\int_{\Delta E_{g'}} dE'\,\Phi(E')}\tag{55}$$

The bin-to-bin cross section is a point function in space, a spectrum-weighted average in energy, and an element average in incident direction. It is a bin-integrated function with respect to the secondary energy and the secondary direction. The bin-to-bin cross section has units of *barns*.

Appendix B: Summary of FORTRAN 90/95 Syntax Terms

A more complete presentation of FORTRAN 90/95 syntax can be found in reference (7).

- *Allocatable* Array

  An array whose shape and size are not determined until space is created for the array by means of an allocate

- *Allocate*(array( ))

  Command the creates an array at execution

- *Call* mysub( )

  A call to user-defined subroutine, mysub

- *Close*(myfile)

  A command to close a file previously opened for I/O

- *Cycle*

  A command to execute the next loop in a Do constuct

- *Do...End Do*

  A loop initiated by Do and terminated by End Do

- Derived *Type*

  A programmer-defined variable type, typically a compound of other intrinsic types

- Extent

  Number of elements in a particular dimension of an array

- *If( )Then...ElseIf( )...Else...End If*

  A logical construct

- *Open*(myfile)

  A command to open a file for I/O

- *Read*( )

  A command to retrieve information from a file previously opened for input

- *Select Case( )...Case( )...End Select Case( )*

  A logical construct to select from many cases using the same variable

Appendix C: Doppler Broadening

The cross section equations presented in chapter 2 are general enough to include Doppler broadening. The cross section, $s(E\ell)$, in equation (30) changes to $s^*(E\ell T)$, an effective cross section that includes the temperature dependence. The broadening is important to the cross section calculation because the total energy available for the reaction is the important parameter for determining the likelihood of a reaction. Therefore, the energy of the incident neutron and the average energy of the target nuclei, characterized by the material temperature, combine to form a broadened cross section or an effective cross section. This broadening of the cross section is typically called Doppler broadening. If a transport calculation is to be performed at realistic temperatures such as between three hundred to a few thousand degrees Kelvin, then the cross section must be broadened in order for the transport result to be meaningful. Additionally, this research required validation from sources that contained only Doppler broadened data.

Prior to deriving the broadening integral, I assume that the functional dependence of the secondary neutron energy and the angle of scatter of the neutron do not strongly depend on the temperature of the interacting material. This approximation exactly follows the NJOY development (13). The value of the cross section is the only function broadened and the angular and secondary energy distributions remain unaffected by the Doppler broadening.

The effective cross section for a material at temperature T is defined to be that cross section that gives the same reaction rate for a stationary target nuclei as the real cross section gives for moving nuclei. The effective cross section is

$$rv\bar{s}(v,T) = \int d\vec{v}\ell \, |\vec{v} - \vec{v}\ell| s(|\vec{v} - \vec{v}\ell|) P(\vec{v}\ell T) \qquad (56)$$

where $\vec{v}$ is the velocity of the incident neutron, $\vec{v}\ell$ is the velocity of the target, r is the density of the target nuclei, s is the cross section for stationary nuclei, and $P(\vec{v}\ell T)$ is the distribution function for the target nuclei velocities in the laboratory system.

The velocity distribution of the target nuclei can be a very complicated function. For many applications, however, the target motion can be approximated as isotropic

and the distribution of the velocities can be approximated by the Maxwell-Boltzmann function,

$$P\left(\vec{v}',T\right)d\vec{v}' = \frac{a^{3/2}}{p^{3/2}}e^{-av'^2}d\vec{v}'$$ (57)

where $a = \dfrac{M}{2kT}$, k is Boltzmann's constant, and M is the target mass.

Equation (56) can be partially integrated in terms of the relative speed defined as

$$V = \left|\vec{v}' - \vec{v}\right|,$$ (58)

to give the standard Doppler broadened cross section as the sum

$$\bar{s}\left(v,T\right) = s^*\left(v,T\right) - s^*\left(-v,T\right),$$ (59)

with the function defined as

$$s^*\left(v,T\right) = \frac{a^{3/2}}{p^{1/2}v^2}\int_0^{\yen} dV\, s\left(V\right)V^2 e^{-a(v-V)^2}.$$ (60)

The exponential function in equation (60) limits the significant part of the integral to the range

$$v - \frac{4}{\sqrt{a}} < V < v + \frac{4}{\sqrt{a}}.$$ (61)

For $s^*\left(-v\right)$, the integral depends only on velocities satisfying

$$0 \pounds V < \frac{4}{\sqrt{a}}.$$ (62)

Because all of the data used in the ENDF/B-VI are given energy, rather than velocity, these results can be converted to energy units using

$$E_m = \frac{1}{2}m\left(\frac{4}{\sqrt{a}}\right)^2 = \frac{16kT}{A}.$$ (63)

The numerical evaluation of equation (60) developed for NJOY and used in this dissertation assumes that the cross section can be represented by a piecewise linear function of energy to acceptable accuracy. A piecewise linear function to represent the resonance regions was generated to satisfy this need. The method used to generate the piecewise linear function representation was a simple bisection method. Having generated a piecewise linear representation, equation (60) was evaluated using the following procedure.

Using the subscripts in the following derivations to denote the piecewise linear values obtained for the resonance regions and defining the reduced variables $y = \sqrt{a}v$ and $x = \sqrt{a}v$, the cross section becomes

$$s(x) = s_i + s_i'\left(x^2 - x_i^2\right), \tag{64}$$

with slope

$$s_i' = \frac{\left(s_{i+1} - s_i\right)}{\left(x_{i+1}^2 - x_i^2\right)}. \tag{65}$$

Equation (60) can now be written as

$$s^*(y) = \frac{1}{\sqrt{\pi}y^2}\sum_{i=0}^{N}\int_{x_i}^{x_{i+1}} dx\, s(x)x^2 e^{-(x-y)^2} = \sum_i \left\{A_i\left[s_i - s_i'x_i^2\right] + B_i s_i'\right\}, \tag{66}$$

where

$$x_o = 0 \tag{67}$$

$$x_{N+1} = \yen, \tag{68}$$

$$A_i = \frac{1}{y^2}H_2 + \frac{2}{y}H_1 + H_0, \tag{69}$$

$$B_i = \frac{1}{y^2}H_4 + \frac{4}{y}H_3 + 6H_3 + 4yH_1 + y^2 H_0, \tag{70}$$

and where H_n is shorthand for $H_n\left(x_i - y, x_{i+1} - y\right)$. The extrapolations to zero and infinity assume a constant cross section $\left(s_0 = s_N = 0\right)$. The H functions are the incomplete probability integrals defined by

$$H_n(a,b) = \frac{1}{\sqrt{\pi}}\int_a^b dz\, z^n e^{-z^2}. \tag{71}$$

These functions can be computed by

$$H_n(a,b) = F_n(|a|) - F_n(|b|), \tag{72}$$

where

$$F_n(a) = \frac{1}{\sqrt{\pi}}\int_a^{\yen} dz\, z^n e^{-z^2}. \tag{73}$$

The F_n functions satisfy a recursion relation that can be used to obtain

75

$$F_0(a) = \frac{1}{2} \text{erfc}(a),\tag{74}$$

$$F_1(a) = \frac{1}{2\sqrt{p}} \exp(-a^2),\tag{75}$$

$$F_n(a) = \frac{n-1}{2} F_{n-2}(a) + a^{n-1} F_1(a),\tag{76}$$

and where the $\text{erfc}(a)$ denotes the complementary error function

$$\text{erfc}(a) = \frac{2}{\sqrt{p}} \int_a^{\yen} dz\, e^{-z^2}.\tag{77}$$

Appendix D: Energy Group Structures

All of the energy group structures used throughout the dissertation are documented here. The values are all in eV and are displayed using the FORTRAN exponential notation. The values displayed are the energy group boundaries.

D.1: LANL-30

1.70E+7	3.68E+6	3.03E+5	4.54E+2	4.14E-1
1.50E+7	2.87E+6	1.84E+5	1.67E+2	1.52E-1
1.35E+7	2.23E+6	6.76E+4	6.14E+1	1.39E-4
1.20E+7	1.74E+6	2.48E+4	2.26E+1	
1.00E+7	1.35E+6	9.12E+3	8.32E00	
7.79E+6	8.23E+5	3.35E+3	3.06E00	
6.07E+6	5.00E+5	1.24E+3	1.13E00	

D.2: ALTERED LANL-30

This energy group structure is identical to the LANL-30 shown above except that the highest energy groups has been replaced with a group containing 14.0 to 14.1 MeV neutrons. The second energy group has also changed to accommodate the new highest energy group.

1.41E+7	3.68E+6	3.03E+5	4.54E+2	4.14E-1
1.40E+7	2.87E+6	1.84E+5	1.67E+2	1.52E-1
1.35E+7	2.23E+6	6.76E+4	6.14E+1	1.39E-4
1.20E+7	1.74E+6	2.48E+4	2.26E+1	
1.00E+7	1.35E+6	9.12E+3	8.32E00	
7.79E+6	8.23E+5	3.35E+3	3.06E00	
6.07E+6	5.00E+5	1.24E+3	1.13E00	

D.3: NEW 59 GROUP STRUCTURE

This group structure is based on the altered LANL-30 presented above except that each energy group has been cut into two pieces using the geometric mean. The formula is the square root of the product of the energy group boundaries. The highest energy group has not been cut into two pieces.

1.41E+7	3.68E+6	3.03E+5	4.54E+2	4.14E-1
	3.249862E+6	2.361186E+5	2.753507E+2	2.508545E-1
1.40E+7	2.87E+6	1.84E+5	1.67E+2	1.52E-1
1.374773E+7	2.529842E+6	1.115276E+5	1.012610E+2	4.596520E-3
1.35E+7	2.23E+6	6.76E+4	6.14E+1	1.39E-4
1.272792E+7	1.969822E+6	4.094484E+4	3.725104E+1	
1.20E+7	1.74E+6	2.48E+4	2.26E+1	
1.095445E+7	1.532645E+6	1.503915E+4	1.371248E+1	
1.00E+7	1.35E+6	9.12E+3	8.32E00	
8.826098E+6	1.054064E+6	5.527386E+3	5.045711E+00	
7.79E+6	8.23E+5	3.35E+3	3.06E00	
6.876431E+6	6.414827E+5	2.038136E+3	1.859516E+00	
6.07E+6	5.00E+5	1.24E+3	1.13E00	
4.726267E+6	3.892300E+5	7.503066E+2	6.839737E-1	

D.4: New 117 Group Structure

This group structure is based on the new 59 group structure presented above except that each energy group has been cut into two pieces using the geometric mean. The formula is the square root of the product of the energy group boundaries. The highest energy group has not been cut into two pieces.

1.41E+7	3.68E+6	3.03E+5	4.54E+2	4.14E-1
	3.458250E+6	2.674770E+5	3.535664E+2	3.222635E-1
	3.249862E+6	2.361186E+5	2.753507E+2	2.508545E-1
	3.054031E+6	2.084366E+5	2.144378E+2	1.952687E-1
1.40E+7	2.87E+6	1.84E+5	1.67E+2	1.52E-1
1.387329E+7	2.694559E+6	1.432518E+5	1.300407E+2	2.643239E-2
1.374773E+7	2.529842E+6	1.115276E+5	1.012610E+2	4.596520E-3
1.362330E+7	2.375194E+6	8.682895E+4	7.885065E+1	7.993224E-3
1.35E+7	2.23E+6	6.76E+4	6.14E+1	1.39E-4
1.310828E+7	2.095878E+6	5.261056E+4	4.782482E+1	
1.272792E+7	1.969822E+6	4.094484E+4	3.725104E+1	

1.235860E+7	1.851348E+6	3.186584E+4	2.901506E+1	
1.20E+7	1.74E+6	2.48E+4	2.26E+1	
1.146531E+7	1.633035E+6	1.931246E+4	1.760403E+1	
1.095445E+7	1.532645E+6	1.503915E+4	1.371248E+1	
1.046635E+7	1.438426E+6	1.171141E+4	1.068119E+1	
1.00E+7	1.35E+6	9.12E+3	8.32E00	
9.394732E+6	1.192890E+6	7.099983E+3	6.479222E+00	
8.826098E+6	1.054064E+6	5.527386E+3	5.045711E+00	
8.291882E+6	9.313939E+5	4.303109E+3	3.929361E+00	
7.79E+6	8.23E+5	3.35E+3	3.06E00	
7.318975E+6	7.265950E+5	2.612997E+3	2.385397E+00	
6.876431E+6	6.414827E+5	2.038136E+3	1.859516E+00	
6.460645E+6	5.663403E+5	1.589745E+3	1.449570E+00	
6.07E+6	5.00E+5	1.24E+3	1.13E00	
5.356159E+6	4.411519E+5	9.645622E+2	8.791418E-1	
4.726267E+6	3.892300E+5	7.503066E+2	6.839737E-1	
4.170451E+6	3.434191E+5	5.836430E+2	5.321326E-1	

Appendix E: Discrete Ordinates Quadrature Sets

The discrete ordinates for a Gauss-Legendre quadrature values are taken directly from Lewis and Miller (7). The directions are given for a one-dimensional transport calculation and the weights sum to 2. The discrete ordinates are symmetric around $m = 0$ and only tabulated for $m > 0$.

m_n	w_n
0.5773502691	1.0000000000

Table 3: S_2 level symmetric directions and weights

m_n	w_n
0.3399810435	0.6521451549
0.8611363115	0.3478548451

Table 4: S_4 level symmetric directions and weights

m_n	w_n
0.2386191860	0.4679139346
0.6612093864	0.3607615730
0.9324695142	0.1713244924

Table 5: S_6 level symmetric directions and weights

m_n	w_n
0.1252334085	0.2491470458
0.3678314989	0.2334925365
0.5873179542	0.2031674267
0.7699026741	0.1600783286
0.9041172563	0.1069393260
0.9815606342	0.0471753364

Table 6: S_{12} level symmetric directions and weights

m_n	w_n
0.0337652428	0.08566224618
0.1693953067	0.1803807865
0.3806904069	0.2339569672
0.6193095930	0.2339569672
0.8306046932	0.1803807865
0.9662347571	0.08566224618

Table 7: DS_6 double level symmetric directions and weights

Appendix F: ENDF/B-VI Data Representations

The ENDF/B-VI documentation (18) allows for many different specific representations. These fill in the appropriate cases presented in chapter 3. The primary advantage of working directly with the ENDF/B-VI representations is that no other intermediate approximations have been used prior to calculating the group-to-group cross sections. The implemented, neutron-producing reactions are presented below.

Cross section representation
    Tabular
    Histogram
    Linear x, linear y
    Linear x, log y
    Log x, linear y
    Log x, log y
    Parameterized (resonance regions)
        Isotope dependence
        Single-level Breit-Wigner
        Multi-level Breit-Wigner
        Reich-Moore
    Unresolved resonance regions
        All parameters energy dependent
        Fission parameters energy dependent
        No parameters energy dependent
Independent angular distributions
    Frame of reference
    Center of mass
    Laboratory frame
    Representations
        Legendre polynomial expansion of the scatter cosine
        Tabular approximation of the scatter cosine
        Two energy ranges Legendre and tabular
        Isotropic
Independent energy distributions (laboratory frame only)
    Representations
        Tabular
        Generalized evaporation spectrum
        Simple fission spectrum
        Evaporation spectrum
        Energy dependent Watt spectrum
Dependent energy and angular distributions
    Frame of reference
        Center of mass
        Laboratory
    Representations
        Continuum energy-angle distribution

Legendre coefficients
Tabulated function
Discrete two-body scattering
Isotropic discrete emission
N-body phase space distribution
Laboratory angle-energy distribution
Energy dependent fission neutron production

Appendix G: Sample Input Files

Sample input files are given for the various programs that create, manipulate, and ultimately use the cross section data. The three programs created specifically for this dissertation are the cross section integrator for neutrons, the converter to macroscopic cross sections, and the one-dimensional transport code capable of using five different discrete spatial quadrature methods.

G.1: CROSS SECTION INTEGRATOR SAMPLE FILE

```
&XSINNml
    ENDFName = "I:\XSINRunFolder\InputFiles\B10.txt"
    enGroupName = "I:\XSINRunFolder\InputFiles\AltLANL30Grp.txt"
    outputDirectory = "I:\DissTest2\30Groups\B10\"
    outputFile = "ScatB10_30"
! include discrete elements
    discreteElements = .FALSE.
    DEName = "c:\XSIN\Input\h_1D2.txt"
! include legendre moments for validation
    LegendreMoments = .FALSE.
    numberMoments = 5
! include average tabular values
    averageTabular = .TRUE.
! factors of two to use in [-1,1] total == 2**numberTabular
    numberTabular = 7
    enableDiagnostic = .TRUE.
    desTol = 0.001
    absoluteTol = 1.E-25
    enSpectralType = "One_over_E"
    mechanisms = 2, 5, 11, 16, 17, 18, 21, 22, 23, 24, 25, 29, 30, 32, 33, 34, 35, 36,
37, 38, 41, 42, 44, 45, 51, 52, 53, 54, 55, 56, 57, 58, 59, 60, 61, 62, 63, 64, 65, 66,
67,68, 69, 70, 71, 72, 73, 74, 75, 76, 77, 78, 79, 80, 81, 82, 83, 84, 85, 86, 87, 88,
89,90, 91
    temperature = 300
/
&DiagnosticNml
    doAllGroups = .TRUE.
    startIncEnGroup = 1
    endIncEnGroup = 30
    startSecEnGroup = 1
    endSecEnGroup = 30
    outputExcelStyle = .FALSE.
    outputMMAStyle = .FALSE.
    outputEachMechanism = .FALSE.
/
```

```
&IntegrateTabNml
! check whether to create the discrete elements cross sections
    createDiscreteElem = .FALSE.
! check whether to create the Legendre moments cross sections
    createLegendreMom = .FALSE.
! check whether to unfold the unique pairings to create the
! complete discrete elements bin-to-bin four dimensional array
    DEInformationFile = "i:\DEHEval\H_1D12.txt"
! location for the output and the base name for the output
    outputDirectory = "i:\DissTest1\MixedXS\Total\"
    outputBaseFile = "H20Tot_30"
/
&MixerNml
    mixerDefinition = "Mixing"
! the only possible types are "Scatter" and "Total"
    xSectType = "Total"
! the number of elements to be mixed
    numElements = 2
! the total number of isotopes to be read in
    totNumIsotopes = 2
! this value = 1/(cm*barns)
    density = 3.3296047E-2
    numberEnergyGroups = 30
    numberTabular = 7
    numberLegendre = 5
/
&ElementNml
    elementName = "Hydrogen"
    numIsoPerElem = 1
    compoundValue = 2
/
&ElementNml
    elementName = "Oxygen"
    numIsoPerElem = 1
    compoundValue = 1
/
&IsotopeNml
    isotopeFile = "i:\DissTest1\H1_30\Total\TotH1_30Tab.txt"
    referenceElement = "Hydrogen"
    elementAtomPercent = 1.0
/
&IsotopeNml
    isotopeFile = "i:\DissTest1\O16_30\Total\TotO16_30Tab.txt"
    referenceElement = "Oxygen"
    elementAtomPercent = 1.0
/
```

85

```
&ProblemDef
    problemDescription = "MultiLayer Iron-Water-B4C-Lead"
    discRun = .TRUE.
    isotropic = .FALSE.
    domain_Diagnostic = .FALSE.
    numberEnergyGrps = 30
    numberRegions = 4
    numberSources = 1
    numberMaterials = 4
    outLocation = "i:\TestProblem1\TransportRuns\MultiLayer\"
    outBaseFile = "MultiLayer_3June"
/
&DiscreteDef
    ! levelSymQuad is "DE" or "S2", "S4", ...
    levelSymQuad = "DE"
    spatialQuadType = "DD"
    numberRefinements = 0
    LegendreOrder = 0
    tolerance = 0.0001
    ECtolerance = 0.0000001
    ! representation is "BtB" or "Leg"
    representation = "BtB"
    energyGroupFile = "i:\TestProblem1\LANL30Grp.txt"
/
&BoundaryCondDef
    leftBoundCond = "Sym"
    rightBoundCond = "Vac"
/
&RegionDef
    xMin = 0.0
    xMax = 1.25
    matIndex = 1
    regionRefine = 6
    numberMCBounds = 1
/
&RegionDef
    xMin = 1.25
    xMax = 3.75
    matIndex = 2
    regionRefine = 7
    numberMCBounds = 1
/
&RegionDef
    xMin = 3.75
    xMax = 4.0
    matIndex = 3
```

```
    regionRefine = 6
    numberMCBounds = 1
/
&RegionDef
    xMin = 4.0
    xMax = 5.25
    matIndex = 4
    regionRefine = 6
    numberMCBounds = 1
/
&SourceDef
    sourceDescription = "Source MultiLayer"
    materialRegion = 1
    sourceGroup = 1
    sourceStrength = 50.0
/
&MaterialDefDisc
    materialDescription = "Iron"
    scatXSectFile =
"i:\TestProblem1\TransportRuns\MultiLayer\Fe56_DEDE.txt"
    discreteElemFile = "c:\FORTRAN Programs\H_1D\H_1D12.txt"
    totXSectFile =
"i:\TestProblem1\TransportRuns\MultiLayer\Fe56_TotTab.txt"
/
&MaterialDefDisc
    materialDescription = "Water"
    scatXSectFile =
"i:\TestProblem1\TransportRuns\MultiLayer\Water_12DE.txt"
    discreteElemFile = "c:\FORTRAN Programs\H_1D\H_1D12.txt"
    totXSectFile =
"i:\TestProblem1\TransportRuns\MultiLayer\WaterTotTab.txt"
/
&MaterialDefDisc
    materialDescription = "B4C"
    scatXSectFile =
"i:\TestProblem1\TransportRuns\MultiLayer\B4C_DEDE.txt"
    discreteElemFile = "c:\FORTRAN Programs\H_1D\H_1D12.txt"
    totXSectFile =
"i:\TestProblem1\TransportRuns\MultiLayer\B4C_TotTab.txt"
/
&MaterialDefDisc
    materialDescription = "Lead"
    scatXSectFile =
"i:\TestProblem1\TransportRuns\MultiLayer\Pb207_DEDE.txt"
    discreteElemFile = "c:\FORTRAN Programs\H_1D\H_1D12.txt"
    totXSectFile =
"i:\TestProblem1\TransportRuns\MultiLayer\Pb207_TotTab.txt"
/
```

Bibliography

1. C. R. Brennan, R. L. Miller, and K. A. Mathews, "Split-Cell Exponential Characteristic Transport Method for Unstructured Tetrahedral Meshes," *Nuclear Science Engineering*, 138, 26 (2001).

2. J. F. Briesmeister, editor, "MCNP—A General Monte Carlo N-Particle Transport Code", Los Alamos National Laboratory, LA-12625-M, Version 4B, (Mar 1997).

3. R. Borsari, R. Fioresi, and T. Trombetti, "Non-negativity of the Anisotropic Scattering Source in Two-Angle (η, ξ) Transport," *Nuclear Science Engineering*, 112, 301 (1992).

4. R. L. Burden and J. D. Faires, *Numerical Analysis, 6th Edition*, Brooks/Cole Publishing Company, Pacific Grove, CA, (1997).

5. *Compaq Visual FORTRAN, Professional Edition 6.6.0*. Version 6.6.0, IBM, CD-ROM. Computer software. Compaq Computer Corporation, 2000.

6. J. A. Dahl, "A Non-Linear Method for Representing the Scattering Cross Section for Discrete Ordinates," presented at Joint Int. Conf. Mathematical Methods and Supercomputing for Nuclear Applications, Saratoga Springs, New York, October 6-10, 1997 (unpublished).

7. J. M. DelGrande and K. A. Mathews, "Nonnegative Anisotropic Group Cross Sections: A Hybrid Monte Carlo-Discrete Elements-Discrete Ordinates Approach", *Nuclear Science and Engineering*, v. 139, p. 33-46, (2001).

8. T. M. R. Ellis, I. R. Phillips, T. M. Lahey, *Fortran 90 Programming*, Addison-Wesley Publishing Company Inc., Harlow, England, (1996).

9. J. M. Hammersley and D. C. Handscomb, *Monte Carlo Methods*, Barnes & Noble, Inc., New York, (1965).

10. E. E. Lewis and W. F. Miller, *Computational Methods of Neutron Transport*, American Nuclear Society, Inc., La Grange Park, IL, (1993).

11. I. Lux and L. Koblinger, *Monte Carlo Particle Transport Methods: Neutron and Photon Calculations*, CRC Press, Boca Raton, (1990).

12. R. E. MacFarlane, "TRANSX 2: A Code for Interfacing MATXS Cross-Section Libraries to Nuclear Transport Codes", LA-12312-MS, Los Alamos National Laboratory, (July 1992).

13. R. E. MacFarlane and D. W. Muir, "The NJOY Nuclear Data Processing System, Version 91", LA-12740-M, Los Alamos National Laboratory, (1994).

14. K. A. Mathews, personal communication, February 2002.

15. K. A. Mathews and C. R. Brennan, "Exponential Characteristic Nonlinear Radiation Transport Method for Unstructured Grids of Triangular Cell," *Nuclear Science Engineering*, 126, 264 (1997).

16. K. A. Mathews, G. E. Sjoden, and B. M. Minor, "Exponential Characteristic Spatial Quadrature for Discrete Ordinates Radiation Transport in Slab Geometry," *Nuclear Science Engineering*, 118, 24 (1994).

17. B. M. Minor and K. A. Mathews, "Exponential Characteristic Spatial Quadrature for Discrete Ordinates Radiation Transport with Rectangular Cells," *Nuclear Science Engineering*, 120, 165 (1995).

18. V. McLane and others, "ENDF-102 Data Formats and Procedures for the Evaluated Nuclear Data File ENDF-6", BNL-NCS-44945-01/04-Rev., (revised April 2001).

19. National Nuclear Data Center, Brookhaven National Laboratory, www.nndc.bnl.gov/nndc/endf/, (2002).

20. I. Stakgold, *Green's Functions and Boundary Value Problems, Second Edition*, John Wiley & Sons, Inc., New York, NY, (1998).

21. T-2 Nuclear Information Service, Los Alamos National Laboratory, t2.lanl.gov/homepage.html, (2002).

REPORT DOCUMENTATION PAGE

Form Approved
OMB No. 074-0188

1. REPORT DATE *(DD-MM-YYYY)* 24-07-2002	2. REPORT TYPE **Doctoral Dissertation**	3. DATES COVERED *(From – To)* April 1999 – July 2002

4. TITLE AND SUBTITLE Efficient and Accurate Computation of Non-Negative Anisotropic Group Scattering Cross Sections for Discrete Ordinates and Monte Carlo Radiation Transport	5a. CONTRACT NUMBER
	5b. GRANT NUMBER
	5c. PROGRAM ELEMENT NUMBER
6. AUTHOR(S) Gerts, David, W., Captain, USAF	5d. PROJECT NUMBER
	5e. TASK NUMBER
	5f. WORK UNIT NUMBER

7. PERFORMING ORGANIZATION NAMES(S) AND ADDRESS(S) Air Force Institute of Technology Graduate School of Engineering and Management (AFIT/EN) 2950 P Street, Building 640 WPAFB OH 45433-7765	8. PERFORMING ORGANIZATION REPORT NUMBER AFIT/DS/ENP/02-4

9. SPONSORING/MONITORING AGENCY NAME(S) AND ADDRESS(ES) Air Force Technical Applications Center ATTN: Maj Jeremy Holtgrave AFTAC Patrick AFB, FL 32925 Phone: (DSN) 854-7946	10. SPONSOR/MONITOR'S ACRONYM(S)
	11. SPONSOR/MONITOR'S REPORT NUMBER(S)

12. DISTRIBUTION/AVAILABILITY STATEMENT

APPROVED FOR PUBLIC RELEASE; DISTRIBUTION UNLIMITED.

13. SUPPLEMENTARY NOTES

14. ABSTRACT

A new method for approximating anisotropic, multi-group scatter cross sections for use in discretized and Monte Carlo multi-group neutron transport is presented. The new method eliminates unphysical artifacts such as negative group scatter cross sections and falsely positive cross sections. Additionally, when combined with the discrete elements angular quadrature method, the new cross sections eliminate the lack of angular support in the discrete ordinates quadrature method.

The new method generates piecewise-average group-to-group scatter cross sections. The accuracy and efficiency for calculating the discrete elements cross sections has improved by many orders of magnitude compared to DelGrande and Mathews previous implementation. The new cross sections have extended the discrete elements method to all neutron-producing representations in the Evaluated Nuclear Data Files.

The new cross section method has been validated and tested with the cross section generation code, NJOY. Results of transport calculations using discrete elements, discrete ordinates, and Monte Carlo methods for two, one-dimensional slab geometry problems are compared.

15. SUBJECT TERMS

Boltzmann Equation, Neutron Transport Theory, Numerical Methods, Radiation Transport, Radiation Shielding, Anisotropic Scattering, Multigroup Theory

16. SECURITY CLASSIFICATION OF:			17. LIMITATION OF ABSTRACT	18. NUMBER OF PAGES	19a. NAME OF RESPONSIBLE PERSON Mathews, Kirk A., Dr
a. REPORT	b. ABSTRACT	c. THIS PAGE	UU	136	19b. TELEPHONE NUMBER *(Include area code)* (937) 255-3636, ext 4508; e-mail: Kirk.Mathews@afit.edu
U	U	U			

Standard Form 298 (Rev. 8-98)
Prescribed by ANSI Std. Z39-18